REPORT NO. FRA/ORD-80/29

ANALYTICAL METHODS FOR FREIGHT CAR/TRUCK DYNAMIC PROBLEMS

July 1980

MARTIN MARIETTA

P. O. Box 179
Denver, Colorado 80201

Prepared for:
U.S. DEPARTMENT OF TRANSPORTATION
Federal Railroad Administration
Office of Research and Development
Washington, D.C. 20590

Technical Report Documentation Page

1. Report No.
FRA/ORD-80/29

2. Government Accession No.

3. Recipient's Catalog No.
PB80 219389

4. Title and Subtitle
ANALYTICAL METHODS FOR FREIGHT
CAR/TRUCK DYNAMIC PROBLEMS

5. Report Date
July 1980

6. Performing Organization Code

7. Author(s) Martin Marietta Corporation
Analytical Mechanics Section

8. Performing Organization Report No.
MCR-80-531

9. Performing Organization Name and Address
Martin Marietta Corporation
P.O. Box 179
Denver, Colorado 80201

10. Work Unit No. (TRAIS)

11. Contract or Grant No.
NAS8-29882

12. Sponsoring Agency Name and Address
Department of Transportation
Federal Railroad Administration (FRA)
Office of Research and Development
Washington, D.C. 20590

13. Type of Report and Period Covered
Technical Report
March 1974-August 1980

14. Sponsoring Agency Code
RRD-11

15. Supplementary Notes

16. Abstract

The analytical methods used to synthesize mathematical models of an 80-ton open hopper railroad car are presented in this report. The work described herein was performed as part of the Track-Train Dynamics program by the Analytical Mechanics Section, Martin Marietta Corporation, Denver Division. This effort was directed toward accurately characterizing the dynamic behavior of this specific railcar configuration. In a larger sense, model formulation and solution using the methods detailed here serve as a potential approach to the characterization of other railcar configurations. The report details the formulation of a nonlinear model including the carbody, trucks, and wheel/rail interactions. In particular hunting stability of the railcar was investigated, and analytical results were compared to actual test data. Test/analytical correlation was very good.

17. Key Words
Railcar modelling,
Rail car/truck dynamics,
Test/analytical correlation,
Hunting stability,
Dynamic modelling

18. Distribution Statement
Document is available to the public
through the National Technical
Information Service, Springfield,
VA 22161

19. Security Classif. (of this report)
Unclassified

20. Security Classif. (of this page)
Unclassified

21. No. of Pages

22. Price

Form DOT F 1700.7 (8-72) Reproduction of completed page authorized

METRIC CONVERSION FACTORS

Approximate Conversions to Metric Measures

Symbol	When You Know	Multiply by	To Find	Symbol
		LENGTH		
in	inches	*2.5	centimeters	cm
ft	feet	30	centimeters	cm
yd	yards	0.9	meters	m
mi	miles	1.6	kilometers	km
		AREA		
in^2	square inches	6.5	square centimeters	cm^2
ft^2	square feet	0.09	square meters	m^2
yd^2	square yards	0.8	square meters	m^2
mi^2	square miles	2.6	square kilometers	km^2
	acres	0.4	hectares	ha
		MASS (weight)		
oz	ounces	28	grams	g
lb	pounds	0.45	kilograms	kg
	short tons (2000 lb)	0.9	tonnes	t
		VOLUME		
tsp	teaspoons	5	milliliters	ml
Tbsp	tablespoons	15	milliliters	ml
fl oz	fluid ounces	30	milliliters	ml
c	cups	0.24	liters	l
pt	pints	0.47	liters	l
qt	quarts	0.95	liters	l
gal	gallons	3.8	liters	l
ft^3	cubic feet	0.03	cubic meters	m^3
yd^3	cubic yards	0.76	cubic meters	m^3
		TEMPERATURE (exact)		
°F	Fahrenheit temperature	5/9 (after subtracting 32)	Celsius temperature	°C

---

*1 in = 2.54 (exactly). For other exact conversions and more detailed tables, see NBS Misc. Publ. 286, Units of Weights and Measures, Price $2.25, SD Catalog No. C13.10:286.

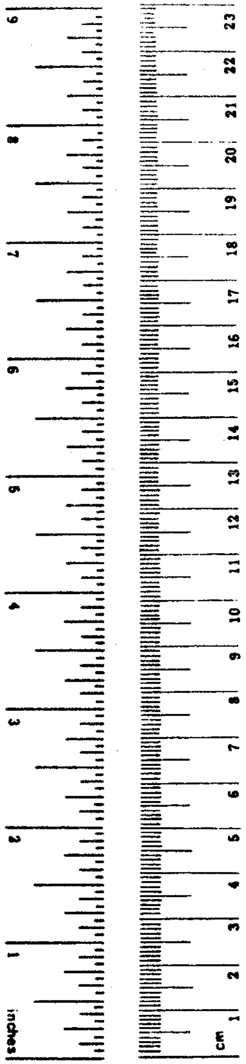

Approximate Conversions from Metric Measures

Symbol	When You Know	Multiply by	To Find	Symbol
		LENGTH		
mm	millimeters	0.04	inches	in
cm	centimeters	0.4	inches	in
m	meters	3.3	feet	ft
m	meters	1.1	yards	yd
km	kilometers	0.6	miles	mi
		AREA		
cm^2	square centimeters	0.16	square inches	in^2
m^2	square meters	1.2	square yards	yd^2
km^2	square kilometers	0.4	square miles	mi^2
ha	hectares (10,000 m^2)	2.5	acres	
		MASS (weight)		
g	grams	0.035	ounces	oz
kg	kilograms	2.2	pounds	lb
t	tonnes (1000 kg)	1.1	short tons	
		VOLUME		
ml	milliliters	0.03	fluid ounces	fl oz
l	liters	2.1	pints	pt
l	liters	1.06	quarts	qt
l	liters	0.26	gallons	gal
m^3	cubic meters	35	cubic feet	ft^3
m^3	cubic meters	1.3	cubic yards	yd^3
		TEMPERATURE (exact)		
°C	Celsius temperature	9/5 (then add 32)	Fahrenheit temperature	°F

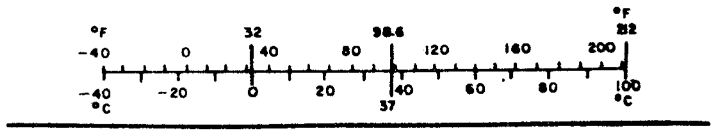

TABLE OF CONTENTS

Page

1.0 SUMMARY 1

2.0 INTRODUCTION 3
2.1 Objective and Approach 3
2.2 Organization of Material 3

3.0 MODELING CONCEPTS 3
3.1 General Considerations 3
3.2 Building Block Approach 4
3.3 Elements of a Dynamic Model 5
3.4 Normal Modes 8
3.5 The Unforced Equation of Motion 10

4.0 MODELING THE BUILDING BLOCKS 11
4.1 Linear Carbody Model 11
  4.1.1 Description of Hardware 11
  4.1.2 Preliminary Conceptualization 11
  4.1.3 Finite Element Mass and Stiffness 14
  4.1.3.1 Carbody Stiffness 14
  4.1.3.2 Carbody Mass 14
  4.1.3.3 Rigid Body Checks 16
  4.1.4 Concept of Modal Coordinates 16
  4.1.5 Model of Modal Survey Data 17
4.2 Truck Model 22
  4.2.1 Description of Hardware 22
  4.2.2 Preliminary Conceptualization of Truck Model 23
  4.2.3 Truck Modal Coordinates 26
  4.2.4 Measurement of Truck Model Parameters 28

5.0 THE FORCING FUNCTIONS 31
5.1 Wheel-Rail Interaction Forces 31
5.2 Generation of Rail Displacement Time History 35

6.0 Coupled System Evaluation 38
6.1 Coupled Equations of Motion 39
6.2 Response to Rail Irregularities 39

7.0 HUNTING STABILITY ANALYSES 42

8.0 CONCLUSIONS AND RECOMMENDATIONS 47

REFERENCES 48

LIST OF ILLUSTRATIONS

Figure		Page
3-1	Rail Vehicle Characterization Analysis/Test Flow Chart	5
3-2	Nonlinear Force-Deflection Curve	7
3-3	Nonlinear Force-Velocity Curve	10
4-1	80-Ton Hopper Car	11
4-2	Carbody As Idealized Beam	12
4-3	Finite Element Model Centerline View	12
4-4	Finite Element Model Side View	13
4-5	Finite Element Model Top View	13
4-6	Illustration of Natural Modes of Vibration	17
4-7	Preliminary Force Vector Selected to Excite the First Three Fundamental Modes of the Carbody	18
4-8	Test Transfer Function Indicating Lateral Bending Mode	19
4-9	Decay Traces of Lateral Bending Mode	19
4-10	Comparison of Analytical and Experimental Mode Shapes - Empty Car	21
4-11	Typical Freight Truck	22
4-12	ASF Ride Control Truck Joints	23
4-13	Barber and ASF Bolster Side Frame Joint Designs	23
4-14	Schematic of Modeling Procedure	24
4-15	CG Coordinate Systems	25
4-16	Force Deflection Curve for Bottoming-Out-Type Springs	26
4-17	Force Deflection Curve for Sliding Friction	26
4-18	Principal Truck Deflection "Mode" Shapes	27
4-19	Phase Six Setup - Lozenge Mode Racking Loading	29
4-20	Comparison of Analytical and Experimental Hysteresis Results	30
5-1	Geometry of Wheel/Rail Interaction	32
5-2	Geometry for Gravity Spring	35
5-3	Statistical Summarization of Data	36
5-4	Spectral Summarization of Data	37
5-5	Truck Centerline Displacement vs Track Distance	38
6-1	Front Truck, Front Axle Wheel/Rail Lateral Force vs Time, 40.9 mph	40
6-2	Front Truck, Front Axle Lateral Displacement Relative to Rail vs Time, 40.9 mph	40
6-3	Front Truck, Front Axle/Wheel Lateral Force vs Time,54.5 mph	40
6-4	Truck, Front Axle Lateral Displacement Relative to Rail vs Time, 54.5 mph	41
6-5	Front Truck, Front Wheel/Rail Lateral Force vs Time, 68 mph	41
6-6	Front Truck, Front Axle Lateral Displacement Relative to Rail vs Time, 68 mph	41
6-7	Measured Front Truck, Front Axle Displacement Relative to Rail	42
7-1	Car cg Lateral Translation, 60 fps	43
7-2	Car Yaw, 60 fps	43
7-3	Car Roll, 60 fps	43
7-4	Front Truck Lateral Translation, 60 fps	43
7-5	Car Torsion Mode, 4.89 Hz, 60 fps	43
7-6	Front Truck Yaw, 60 fps	43
7-7	Front Truck Warping, 60 fps	44
7-8	Front Truck Relative Lateral, 60 fps	44

Figure Page

7-9 Rear Truck Lateral Translation, 60 fps 44

7-10 Rear Truck Yaw, 60 fps 44

7-11 Rear Truck Warping, 60 fps 44

7-12 Rear Truck Relative Lateral, 60 fps 44

7-13 Equivalent Damping Integrals 46

7-14 Nominal Linear Model Hunting 46

7-15 Roll Mode 47

7-16 Torsion Mode 47

LIST OF TABLES

Table		Page
4-1	Carbody Modal Survey Results	20
4-2	Comparison of Empty Carbody Modal Survey to Analysis	20
4-3	Comparison of Scaled Analytical and Experimental Modal Frequencies	21
4-4	Comparison of Loaded Carbody Modal Survey Frequencies to Analysis Frequencies	22
4-5	Truck Analog Parameters	31

1.0 SUMMARY

The work described here was performed as part of the Track-Train Dynamics program by the Analytical Mechanics group, Martin Marietta Corporation, Denver Division.

The objective of this study was to develop and verify a methodology for describing a mathematical model of an 80-ton open hopper railcar system suitable for characterizing its dynamic properties. The objective was divided into three parts:

1) Modeling and verification of the car body.
2) Modeling and verification of the truck.
3) Verification of the carbody/truck system model.

State-of-the art, finite-element modeling techniques were used to model the car body and vibration testing was conducted to obtain data to verify that model. Both an unloaded (empty) and a loaded (with coal) hopper body were subjected to analysis and test. The unloaded configuration analysis predicted consistently higher frequencies than observed in tests. This discrepancy was attributed to the manner in which the car was built as compared to the drawings that were used as a basis for the finite-element model. Two significant factors were noted: 1) Lack of planarity of the side walls (the bow in the middle amounted to 2 inches), and 2) Lack of continuous welds connecting the sill beam to the car (a continuous weld was assumed in the analysis). In spite of the frequency discrepancy, analytical mode shapes agreed well with test. Therefore, test frequencies were used along with analytical mode shapes to represent the verified unloaded car body model in subsequent car body/truck system analyses.

Analytical stiffness of the loaded car body was scaled up to reflect the unloaded configuration test results, but no stiffness adjustment was made to reflect the addition of the coal. Thus, the loaded configuration consisted, in essence, of the test-verified unloaded configuration with the addition of the coal mass. This model predicted lower frequencies than test in the first two modes, but higher than test in the third mode. This discrepancy was attributed to an evident contribution of stiffness by the coal lading. Again, analytical mode shapes showed good correlation with test results. Therefore, the anticipated difficulties associated with improvement of the coal modeling were avoided by using test frequencies along with analytical mode shapes to represent the verified loaded car body model in subsequent car body/truck system analyses. It was concluded that state-of-the art, finite-element modeling is a satisfactory methodology for characterizing railcar mode shapes. However, frequency description will generally require some simple vibration test because of the effects of lading and/or wear on stiffness.

The first attempt at truck modeling was to define a mathematical analog of each joint, i.e. axle to sideframe or bolster to sideframe, and describe potential and dissipated energy at each joint in terms of rigid-body motion of truck members, i.e., sideframes, axles, and bolster, and the centers of gravity (CG). Kinetic energy was to be described in terms of these cg velocities. Application of Lagrange's equation to these energy terms would then provide the equations of motion, or model, of the truck. This modeling effort revealed that individual joint modeling is not practical. Consequently, an alternate approach was taken whereby principal deflection shapes of the truck were assumed and subsequently verified by test. Kinetic energy was described in terms of these shapes and a mathematical analog was defined to describe potential and dissipated energy in terms of these shapes. Finally, an iterative approach was used to find the values of the analog parameters that best represented the test results. These analog parameters were used to represent the verified truck model in all subsequent analyses of carbody/truck system.

It was concluded that the analog developed provides a satisfactory methodology for characterizing truck dynamic properties. However, due to their highly nonlinear nature, the parameters of the analog can be determined only by test.

The last subobjective, verification of the car body/truck system model, required development of the mathematical description of wheel-rail interaction forces to allow model excitation similar to that occurring under operational conditions. This addition introduced forward velocity as a parameter of the model. Two approaches to this verification were taken.

1) A description of rail irregularities, reflecting statistically reduced operational test data was applied, through the wheel-rail interaction description, to the coupled car body/truck models in the time domain. Resulting analytical transients were compared to corresponding operational test data. Because of the statistical handling of test data, direct time correlation of results is not possible. However, the envelopes of model and test results were of the same order of magnitude. Additional test response data in power spectral data (PSD) and standard deviation form is required to improve the quality of this verification step.

2) The coupled car body/truck models were used to predict hunting speeds to compare with observed operational hunting speeds. A linearized version of the model, as well as the full nonlinear car body/truck/wheel-rail interaction model, were used in the hunting study. Initial displacements were imposed on the nonlinear model at various forward speeds. The resulting transient response increased in amplitude from zero to some constant value at all speeds analyzed. This phenomenon, sometimes called limit cycling, indicates potential of the model to hunt at all speeds. Complex eigensolutions for the linearized model were calculated at several speeds. Negative closed-loop damping resulted in some modes at almost all speeds, again indicating the potential of the model to hunt at all speeds.

2.0 INTRODUCTION

2.1 OBJECTIVE AND APPROACH

The objective of this study was to synthesize high-fidelity math models of an 80-ton open top hopper railcar "system" and to verify the models by conducting carefully controlled tests.

A sequential building-block approach, beginning with tractable "subsystems" and culminating with the complete nonlinear railcar system, was chosen to obtain comparative/corrective test and analytical model data. The natural physical separation of the carbody and trucks facilitated this approach. More importantly, the distinct behaviorial differences between these components, i.e., the linear nature of the car and the clearly nonlinear nature of the trucks required different testing and analysis techniques. Finally, assembling these components (literally and mathematically) and experimentally verifying the system model necessitated additional considerations for both test and analysis.

2.2 ORGANIZATION OF MATERIAL

The text is intentionally written to aid analysts unfamiliar with the techniques of dynamic model synthesis. To this end, introductory discussion of what constitutes a "math model", the tradeoffs of model complexity and performance objectives with operational constraints, and the role of test data in model building and verification, is provided in Section 3. After emphasizing the importance of assumptions the analyst must consciously make, focus turns to a general discussion of finite element modeling along with a brief description of normal modes, and their advantages in reducing computation costs.

In Section 4, the specific steps taken to construct the car body finite element model and to arrive at the corresponding linear model natural modes are described. Vibration test data used to verify these modes are presented and compared with analytical results. Similarly, all analytical steps taken to arrive at the truck model are described in Section 4, along with corresponding tests performed to identify numerical values of the model parameters.

Section 5 develops linear expressions for relative velocity induced creep and gravity induced wheel-rail interaction forces. These force terms are then transformed to the truck coordinate system allowing the formulation of the total track train system model.

In Section 6, steps taken to evaluate the track train system model are discussed, while use of the track train system model to predict hunting stability is demonstrated in Section 7. Finally, conclusions and recommendation are presented in Section 8.

3.0 MODELING CONCEPTS

The purpose of this section is to discuss the significant concepts of mathematical models to set the stage for the remainder of this report. This general introduction to math modeling is intended to give perspective to those uninitiated analysts lacking hands-on experience with this tool of engineering analysis.

3.1 GENERAL CONSIDERATIONS

Virtually every physical system confronted by engineering analysts contains interactive processes that defy exact mathematical representation, either because the interdependence of the process variables is not completely understood, or because the available techniques are not sufficiently powerful to describe all system states. Hence, engineering analysis requires that many subjective assumptions be made to permit the mathematical expressions approximating the system process to be written and solved. The selection of analytical technique also lies with the analyst. His choice must be consistent with the range of application of the technique. Simply stated then, a math model may be defined as:

a. A set of assumptions, plus

b. A set of equations consistent with the assumptions.

These two ingredients comprise the mathematical approximation to the real situation.

Several important considerations must be recognized by the analyst before he begins the modeling process. First, he must clearly understand the eventual use of the model in satisfying the objectives of the study. Too often "the model" is taken to be the end-item of his labors, rather than properly applying the information derived by exercising it. A major part of the analyst's job is to translate the results of his analysis using the math model into practical design or corrective information to benefit the physical system hardware in terms of cost or improved performance. To this end, the degree of model complexity that the analyst chooses must be compatible with the accuracy required to meet these goals. The model should be adequate to satisfy these requirements, but model complexity beyond that can be counterproductive and should be avoided.

The complexity required to obtain adequate performance from the model will be limited by the computational resources available to the analyst. Complexity must also be traded off with the time and budget allocated for the analysis. The analyst must choose between the various digital, analog or hybrid (combination digital and analog) computers at his disposal, and must structure the model accordingly. Each of these types of computational schemes has inherent advantages, disadvantages, and operational constraints to be weighed. For instance, large-scale digital computers allow the mathematical model complexity to increase almost without bound, but it does not follow that bigger is better because the understanding gained by the analyst does not necessarily increase with model complexity.

3.2 BUILDING BLOCK APPROACH

Having reconciled these often conflicting elements of model complexity, performance objectives, schedule, and cost, the analyst must then lay out an approach to formulating the mathematical model of the system under study. A "building-block" approach is typically employed whereby the system is broken down into a group of subsystems. The subdivisions, although arbitrary, are usually made on the basis of mathematical expediency and generally follow the "natural" separation of the physical system into its identifiable components. Each of these subsystems can then be handled efficiently by making assumptions about the internal workings of the components and deriving the governing equations that express the assumed interdependence of component variables. Allowance must be made to permit the eventual integration of the subsystem model during this process.

The advantage of this approach is that an interactive hardware test program can be conducted in parallel with modeling activity. Test data are a key ingredient in the mathematical characterization of the physical system being modeled, enhancing the analysts understanding of how system components work, and verifying the adequacy of assumptions and the validity of the mathematical statements that the analyst has made. It should be emphasized that maximum benefit is obtained by integrating the test and analysis activity. Pretest analyses provide insight for designing and conducting the proper tests, and the resultant test data either verifies or modifies the analytical approach.

The building block interactive test analysis approach just described was implemented on this program. Appropriate analytical models and railcar component hardware were used, beginning with two "simple" subsystems and culminating with the complete nonlinear railcar system and its math model analogue. The natural separation of the railcar body and trucks directly facilitated this approach. Most importantly, however, the differences between the linear carbody and the nonlinear trucks clearly required different testing and analysis techniques. The flowchart shown in Figure 3-1 depicts the overall structure of the experimental and analytical sequence used on the program. Each activity is discussed in the following sections.

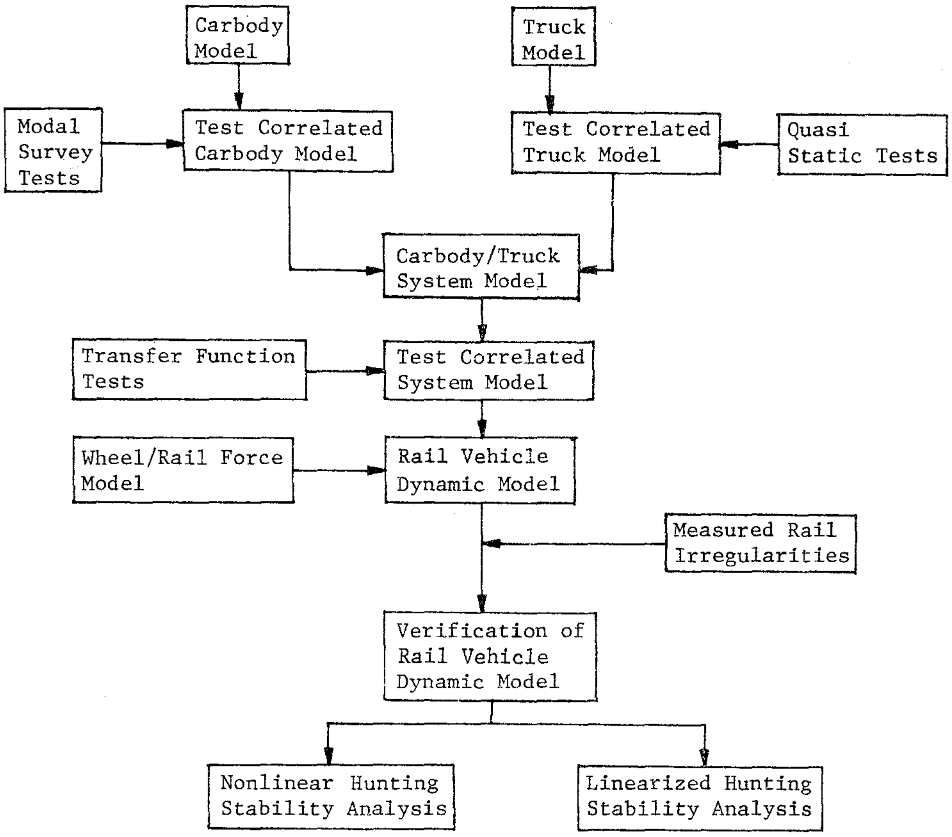

Figure 3-1 Rail Vehicle Characterization Analysis/Test Flow Chart

3.3 ELEMENTS OF A DYNAMIC MODEL

Energy methods by which dynamic models are generated are well known[1]. A broad overview of dynamic modeling techniques is presented here to lay ground work for later development.

In general, a finite element dynamic model is a collection of mathematical simulations of component or subcomponent parts of the structure being considered (i.e., building blocks). Hereafter, these parts will be referred to as elements. The initial step in the simulation is to define the kinetic and potential energy in each of the elements. The general form of these expressions are:

$$\text{Kinetic Energy, } (\text{K.E.})_j = 1/2 \int_{\tau_j} \rho v^2 dV \tag{3-1}$$

$$\text{Potential Energy, } (\text{P.E.})_j = 1/2 \int_{\tau_j} E\varepsilon^2 dV \tag{3-2}$$

where

τ_j = the volume of $j^{\underline{th}}$ structural element

dV = a differential volume

ρ = mass density of the differential volume

v = the velocity of the differential volume

ε = the strain in the differential volume

E = Young's modulus of the differential volume.

---

[1] See References, p. 48.

Exact evaluation of these integrals is seldom, if ever, possible. Usually, they are approximated by assuming constant or linearly varying material properties and by defining velocity and strain throughout the volume, τ_j, as functions of a discrete global coordinate system, $\{h\}$.

For example, if the $j^{\underline{th}}$ element were a rod of length l_j, the velocity might be defined as a linear function between points a and b on the rod. Then

$$V(x) = \dot{h}_a + (\dot{h}_b - \dot{h}_a)\ X/\ell_j \tag{3-3a}$$

which can be represented in matrix form as

$$V(x) = \{T_v(x)\}_j^T\{\dot{h}\} \tag{3-3b}$$

where x is the variable of integration along the rod. If the crossection area of the rod is $A_j\ (x)$, the kinetic energy experssion in terms of the global coordinates becomes

$$\begin{aligned}(KE)_j &= 1/2\ \{\dot{h}\}^T\left[\rho\int_o^{\ell_j} \{T_v(x)\}_j\ A_j(x)\{T_v(x)\}_j^T dx\right]\ \{\dot{h}\}\\ &= 1/2\ \{\dot{h}\}^T[m_j]\ \{\dot{h}\}\end{aligned} \tag{3-4}$$

The corresponding potential energy expression might be developed by defining the strain, ε_j, as constant between points a and b. Then

$$\varepsilon_j = \frac{1}{\ell_j}(h_b - h_a) \tag{3-5a}$$

$$= \{T\}_j^T\{h\} \tag{3-5b}$$

and the potential energy in the global coordinates becomes

$$(PE)_j = 1/2\ \{h\}^T\{\psi\}_j\left(\int_o^{\ell_j} E_jA_j(x)dx\right)\ \{\psi\}_j^T\{h\} \tag{3-6a}$$

$$\equiv 1/2\ \{h\}^T[k_j]\{h\} \tag{3-6b}$$

When all elements of the model possess similar linear characteristics, the energy expressions for the total structure are obtained by addition of the element contributions. That is

$$(K.E.)_{total} = \{\dot{h}\}^T\left(\sum_{j=1}^{n}[m_j]\right)\{\dot{h}\} \equiv \{\dot{h}\}^T[M]\{\dot{h}\} \tag{3-7}$$

$$(P.E.)_{total} = \{\dot{h}\}^T\left(\sum_{j=1}^{n}[k_j]\right)\{h\} \equiv \{h\}^T[K]\{h\} \tag{3-8}$$

where

n = the total number of elements

[M] = the model mass matrix

[K] = the model stiffness matrix

Application of Lagrange's equation[1] may now be used to form the homogeneous equations of motion for the structure as,

$$[M]\{\ddot{h}\} + [K]\{h\} = \{0\} \qquad (3\text{-}9)$$

Unfortunately, not all structures can be well simulated by linear approximations. Usually, when nonlinearities are important, it is the potential energy term that reflects this situation. Dissipated energy, or damping, also reflects nonlinearities. This term will be discussed at the end of this section.

For example if the $\gamma^{\underline{th}}$ element is a loose joint, such as the axle/side frame connection of a rail truck, the forces required to strain the element may be a nonlinear function of that strain. Figure 3-2 presents an example of this situation. The potential energy of such an element is equivalent to the work done by the force, F(ε), moving with the local coordinate, ε. That is,

$$(PE)_\gamma = (Wk)_\gamma = \int F_\gamma(\varepsilon)d\varepsilon \qquad (3\text{-}10)$$

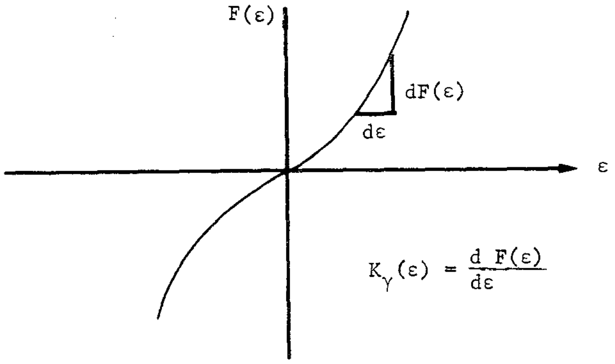

Figure 3-2 Nonlinear Force-Deflection Curve

This term could be cast in a form similar to equation 3-6b and included in the potential summation of equation 3-8. There would be little advantage to doing so since the resulting [K] coefficients would be all constants. A more manageable approach is to use a strain transformation, similar to equation 3-5b, to convert the nonlinear work expression from local to global coordinates as,

$$(Wk)_\gamma = \int F_\gamma\ (\varepsilon)\{\Psi\}_\gamma^T\{dh\} \qquad (3\text{-}11)$$

Differentiating with respect to {h},

$$\frac{d(Wk)_\gamma}{d\{h\}} = \{\psi\}_\gamma F_\gamma(\varepsilon), \qquad (3\text{-}12)$$

gives the displacement dependent forces applied to the global coordinate system. The collection of all nonlinear displacement dependent forces can be written

$$\sum_{\gamma=1}^{R} \{\psi\}_\gamma F_\gamma(\varepsilon) \equiv [\psi]^T\{F(\varepsilon)\} \tag{3-13}$$

Now, the general equation of motion, 3-9, can be modified to reflect both linear and nonlinear structure by,

$$[M]\{\ddot{h}\} + [K]\{h\} = -[\psi]^T\{F\ (\varepsilon)\} \tag{3-14}$$

This equation must be solved simultaneously with the force displacement relationship depicted in Figure 3-2, as expressed in global coordinates. That is,

$$\{F\ (\varepsilon)\} \equiv [k\ (\varepsilon)][\psi]\{h\} \tag{3-15}$$

A more specific description of this approach as applied to the hopper car model can be obtained from equation 3-14 by identifying the car coordinates, $\{h_T\}$, as subsets of $\{h\}$. That is,

$$\{h\} \equiv \begin{Bmatrix} h_c \\ h_T \end{Bmatrix} \tag{3-16}$$

Then, if we further specify that $n=a+b$ in the energy summations of equations 3-7 and 3-8,

$$\{\dot{h}\}^T\left(\sum_{j=1}^{a} [m_j]\right)\{\dot{h}\} \equiv \{\dot{h}_c\}^T[M_c]\{\dot{h}_c\} \tag{3-17a}$$

$$\{h\}^T\left(\sum_{j=1}^{a} [k_j]\right)\{h\} \equiv \{h_c\}^T[K_c]\{h_c\} \tag{3-17b}$$

$$\{\dot{h}\}^T\left(\sum_{j=a+1}^{b} [m_j]\right)\{\dot{h}\} \equiv \{\dot{h}_T\}^T[M_T]\{\dot{h}_T\} \tag{3-17c}$$

$$\{h\}^T\left(\sum_{j=a+1}^{b} [k_j]\right)\{h\} \equiv 0 \tag{3-17d}$$

we can rewrite equation 3-14 as,

$$\left[\begin{array}{c|c} M_c & 0 \\ \hline 0 & M_T \end{array}\right] \begin{Bmatrix} \ddot{h}_c \\ \ddot{h}_T \end{Bmatrix} + \left[\begin{array}{c|c} K_c & 0 \\ \hline 0 & 0 \end{array}\right] \begin{Bmatrix} h_c \\ h_T \end{Bmatrix} = \left[\begin{array}{c|c} \psi_{IC}^T & 0 \\ \hline \psi_{IT}^T & \psi_T^T \end{array}\right] \begin{Bmatrix} F_I(\varepsilon) \\ F_T(\varepsilon) \end{Bmatrix} \tag{3-18}$$

That is: a) The only coupling between car and trucks is due to the nonlinear interface forces, $[\psi_I^T]\ \{F_I(\varepsilon)\}$, between them, b) the car body model is completely linear, and c) the only restoring forces (excluding wheel/rail forces) on the truck model are the nonlinear, $[\psi_T^T]\{F_T(\varepsilon)\}$. It will be shown in Section 4 that the number of coordinates required to describe the car model is large.

3.4 NORMAL MODES

To minimize computer costs, the car body was transformed to modal coordinates using the homogenous equations of motion from the first-row partition of equation 3-18. The advantage of normal modes, as will be shown, is that they transform the model into a set of uncoupled coordinates. Each coordinate is associated with a modal frequency. Therefore, transient analysis can often be conducted using only those coordinates in the frequency range of interest.

One may define the transformation from discrete to normal mode coordinates as,

$$\left\{h_c\right\} = \left[\phi_c\right] \left\{q_c\right\} \tag{3-19}$$

where

$\left[\phi_c\right]$ = the matrix of car model eigenvectors

$\left\{q_c\right\}$ = the normal modes coordinate vector of the car.

The $i^{\underline{th}}$ column, $\left\{\phi_c\right\}_i$, of matrix $\left[\phi_c\right]$ is obtained as the solution of the eigenproblem,

$$\left(-\omega_{c_i}^2\left[M_c\right] + \left[K_c\right]\right)\left\{\phi_c\right\}_i = \{0\} \tag{3-20}$$

There are several methods $^{(1)(2)(3)(4)}$ by which the $i^{\underline{th}}$ mode eigenvalue, $\omega_{c_i}^2$, and eigenvector, $\left\{\phi_c\right\}_i$, can be calculated from equation 3-20. Any method that produces a valid solution for the considered system may be used. All valid solutions produce a set of eigenvectors that are orthogonal with respect to both the mass and stiffness matrices of the system. That is,

$$\left\{\phi_c\right\}_i^T \left[M_c\right]\left\{\phi_c\right\}_k = \begin{bmatrix}\text{Meq}_{ci}\\ 0\end{bmatrix} \text{ when } \begin{bmatrix}i=k\\ i\neq k\end{bmatrix} \tag{3-21}$$

and

$$\left\{\phi_c\right\}_i^T \left[K_c\right]\left\{\phi_c\right\}_k = \begin{bmatrix}\omega_{c_i}^2\text{Meq}_{c_i}\\ 0\end{bmatrix} \text{ when } \begin{bmatrix}i=k\\ i\neq k\end{bmatrix} \tag{3-22}$$

where Meq_{c_i} is often called the generalized mass of the $i^{\underline{th}}$ mode. Substitution of equations 3-19 for h_c in the first row portion of equation 3-18 and premultiplying by $\left[\phi_c\right]^T$ gives,

$$\left[\phi\right]^T \left[M_c\right] \left[\phi\right] \left[\ddot{q}_c\right] + \left[\phi\right]^T \left[K_c\right] \left[\phi\right] \left[q_c\right] = \left[\phi^T\psi_{Ic}^T\right] \left\{F_I(\varepsilon)\right\} \tag{3-23}$$

The orthogonality relationships of equations 3-21 and 3-22 give equation 3-23 the form,

$$\left\lceil \text{Meq}_c \right\rfloor \{\ddot{q}\} + \left\lceil \text{Meq}_c \right\rfloor \left[\omega_c^2\right] \{q\} = \left[\phi^T\psi_{Ic}^T\right] \left\{F_I(\varepsilon)\right\} \tag{3-24}$$

where the symbol $\lceil \quad \rfloor$ specifies a diagonal matrix. Thus, the equations of motion in modal coordinates are uncoupled.

An eigenvector defines the shape, or relative motion, that the discrete coordinate system of the model will display when vibrating freely in a normal mode. The absolute values of the individual numbers in the vector is arbitrary, providing the shape is retained. This attribute allows one to renormalize any eigenvector such that the generalized mass of that mode has a particular value.

In the remaining discussions, all model eigenvectors must be thought of as having been normalized so that all generalized mass values are unity. This normalization makes the "modal stiffness" numerically equal to the eigenvalue. That is, when

$$\left\lceil \text{Meq}_c \right\rfloor = [I]\text{, the unity matrix,} \tag{3-25}$$

it follows from equations 3-21 and 3-23 that,

$$[\phi]^T \left[K_c\right] [\phi] = \left\lceil \omega_c^2 \right\rfloor \tag{3-26}$$

Therefore, substituting equation 3-24 for the first row partition in equation 3-17 gives,

$$\left[\begin{array}{c|c} I & \\ \hline & M_T \end{array}\right] \begin{Bmatrix}\ddot{q}_c\\ \ddot{h}_T\end{Bmatrix} + \left[\begin{array}{c|c} \omega_c^2 & \\ \hline & 0 \end{array}\right] \begin{Bmatrix}q_c\\ h_T\end{Bmatrix} = \left[\begin{array}{c|c} \phi_c^T \quad \psi_{Ic}^T & \\ \hline \psi_{IT}^T & \psi_T^T \end{array}\right] \begin{Bmatrix}F_I(\varepsilon)\\ F_T(\varepsilon)\end{Bmatrix} \tag{3-27}$$

3.5 THE UNFORCED EQUATION OF MOTION

Velocity dependent or damping terms must be added to complete the unforced equations of motion. Mathematical approach to the expression of damping is highly nebulous. For linear systems, damping can be expressed as a linear function of the modal velocity, $2\zeta\omega\dot{q}$, where the ratio, ζ, of actual damping to critical damping, is preferably obtained from test. These are the same tests as those required to verify analytical mode shapes. For nonlinear systems, damping can be obtained only from test. A typical example of nonlinear damping data is depicted by Figure 3-3. The integral

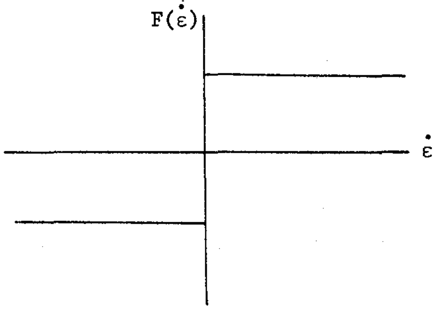

Figure 3-3 Nonlinear Force-Velocity Curve

of the area under the curve in this figure is the power dissipated by the friction force, $F\left(\dot{\varepsilon}\right)$, moving with velocity $\dot{\varepsilon}$.

$$(\text{Power})_\gamma = \int F_\gamma \left(\dot{\varepsilon}\right) d\dot{\varepsilon} \tag{3-28}$$

This term can be expressed in terms of the global coordinate system, as was the work expression of equation 3-11. Differentiating the resulting power with respect to the global velocities $\left\{\dot{h}\right\}$

$$\frac{d\,(\text{Power})_\gamma}{d\left\{\dot{h}\right\}} = \left\{\psi\right\}_\gamma F_\gamma\left(\dot{\varepsilon}\right) \tag{3-29}$$

gives the velocity dependent forces applied to the global coordinate system. The collection of all nonlinear velocity dependent forces can be written

$$\sum_{\gamma=1}^{R} \left\{\psi\right\}_\gamma F_\gamma\left(\varepsilon\right) = \left[\psi\right]^T \left\{F_\gamma\left(\dot{\varepsilon}\right)\right\} \tag{3-30}$$

which is identical in form to equation 3-13.

Now, the final form of the unforced equations can be written by incorporating the linear and nonlinear damping terms into equation 3-27.

That is,

$$\left[\begin{array}{c|c} I & \\ \hline & M_T \end{array}\right] \left\{\begin{array}{c} \ddot{q}_c \\ \hline \ddot{h}_T \end{array}\right\} + \left[\begin{array}{c|c} 2\zeta_c\omega_c & \\ \hline & 0 \end{array}\right] \left\{\begin{array}{c} \dot{q}_c \\ \hline \dot{h}_T \end{array}\right\} + \left[\begin{array}{c|c} \omega_c^2 & \\ \hline & 0 \end{array}\right] \left\{\begin{array}{c} q_c \\ h_T \end{array}\right\}$$

$$= - \left[\begin{array}{c|c} \phi_c^T \; \psi_{Ic}^T & \\ \hline \psi_{IT}^T & \psi_T^T \end{array}\right] \left(\left\{\begin{array}{c} F_I(\varepsilon) \\ \hline F_T(\varepsilon) \end{array}\right\} + \left\{\begin{array}{c} F_I(\dot{\varepsilon}) \\ \hline F_T(\dot{\varepsilon}) \end{array}\right\} \right) \tag{3-31a}$$

which must be solved simultaneously with the corresponding,

$$\left\{F(\varepsilon)\right\} = \left\lceil K_\gamma(\varepsilon) \right\rfloor \left[\psi\right] \left\{h\right\} \tag{3-31b}$$

and

$$\left\{F(\dot{\varepsilon})\right\} = \left\lceil K_\gamma(\dot{\varepsilon}) \right\rfloor \left[\psi\right] \left\{\dot{h}\right\} \tag{3-31c}$$

Specific forms and difficulties encountered in developing equations 3-31 will be identified in the following discussions of the model "blocks". Wheel/rail interface forces that drive the equations of motion will be described in detail in Section 5 of this report.

4.0 MODELING THE BUILDING BLOCKS

4.1 LINEAR CARBODY MODEL

4.1.1 Description of Hardware

A typical 80-ton open hopper car is shown in Figure 4-1. The structure is composed of four stiffened walls, the bottom hopper structure, and a centersill that runs the length of the bottom of the car. The structure is roughly symmetric about midlength. A combination of welded and riveted steel construction is used to fabricate the car. Coal or grain is generally hauled in this type of car.

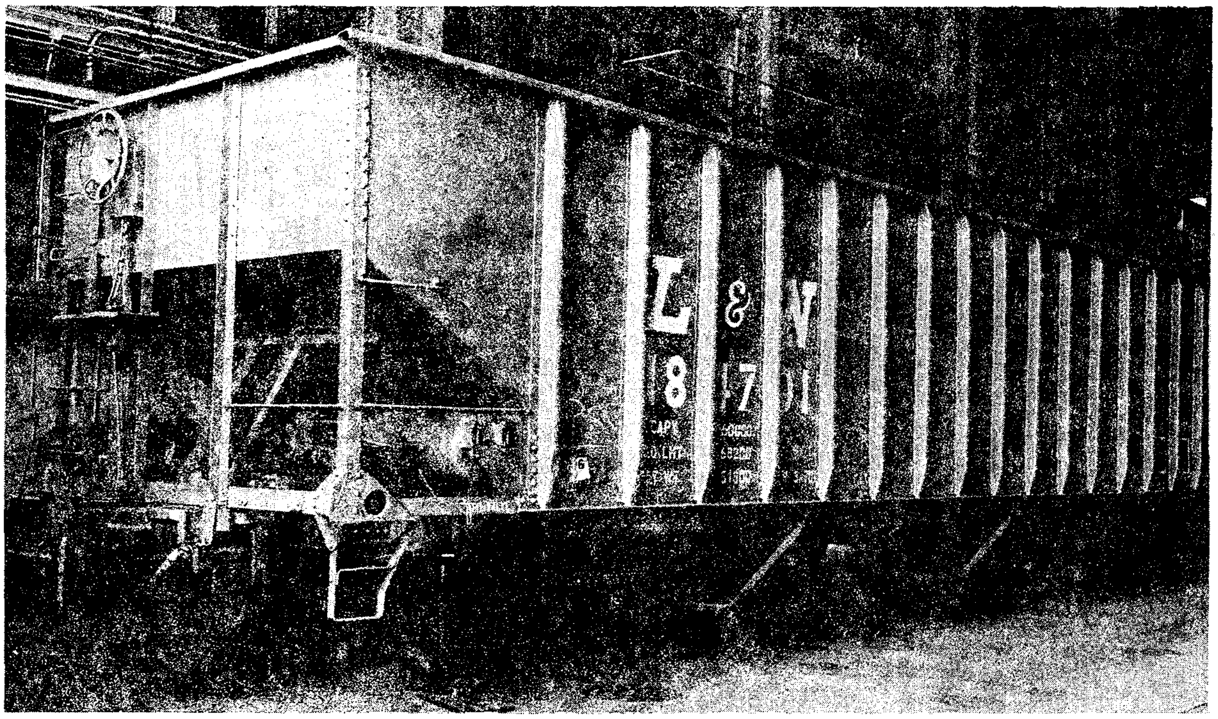

Figure 4-1 80-Ton Hopper Car

4.1.2 Preliminary Conceptualization

A preliminary engineering approach to analyze the dynamic characteristics of the carbody is simple beam theory. If we assume a uniform free-free (or unconstrained) beam for the carbody the fundamental bending frequency can be estimated by the following formula:

$$f_{\text{bending}} = 69\sqrt{\frac{EI}{w\ell^4}} \qquad (4\text{-}1)$$

where E = Young's modulus

w = weight per unit length

I = average moment of inertia about the body plane

ℓ = length of the beam.

We can idealize the carbody, as shown in Figure 4-2, to arrive at the equivalent beam properties. This results in a fundamental frequency of 71 Hz for the first vertical bending mode. It will be shown later that testing of the carbody results in a first vertical bending mode of 29.6 Hz. Obviously, the approximation is too crude for a complex structure

u = Channel Section

w = 35,000 lb

I = 179.6 x 10^3 in^4

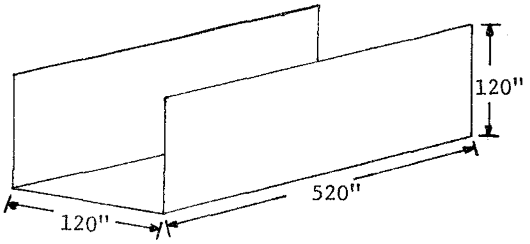

Figure 4-2 Carbody as Idealized Beam

like the carbody. Therefore, we must turn to the more sophisticated (and more expensive) finite element technique to arrive at an accurate engineering model of the carbody.

The symmetry of the carbody about midlength permitted modeling of one-half of the car. The total model was obtained by reflecting the one-half car model about midlength and coupling the two halves together (can be thought of as continuing to add element potential and kinetic energies together).

The centersill beam runs the length of the car and is the primary structure to carry bending loads. Therefore, each half of this beam was modeled in detail with 115 quadrilateral plate elements, spaced at appropriate intervals to allow subsequent attachment of other structural elements, and sized to comply with accepted finite element modeling techniques. Figure 4-3 shows a computer generated front view of this beam. The finite element representation of this beam was compared with closed-form overall beam properties to assure that this important structural member was properly represented.

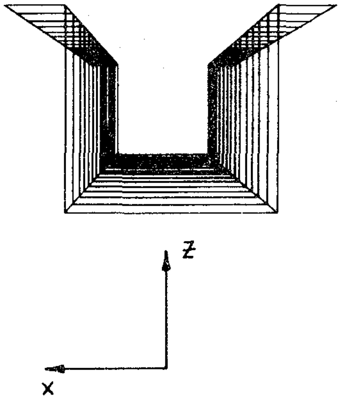

```
B-End Partial Center Sill Beam(HAFSIL2)  Y-Stations 203. to 384.0
Center of Eyes Location    View Point Location     Roll Angle = 0. Deg
                                                   Cone Angle = 20.0 Deg
  X = 0.                     X = 0.                Eye to Eye = 2.0 In
  Y - 5.20000000E+02         Y = 2.93500000E+02
  Z = 9.0.375000E+00         Z = 9.09375000E+00
Run No. = Trial2            Date = 14JN74
```

Figure 4-3 Finite Element Model Centerline View

Many of the structural members used in the construction of this hopper car were standard structural steel shapes. Tabulated properties (from the AISC Steel Manual) were used for these items in the finite element modeling formulation. Structural properties were computed and input for all the nonstandard items, including the centersill filler/centerplate and coupler striker castings. Five finite element types were used in the model generation: planar quadrilateral and triangular plates, axial beams, uniform section bars, and tapered section bars. The bar elements were used to represent members carrying combined axial, bilateral bending shear, and torsion loads.

The resultant detailed stiffness model of one-half car was represented by 355 finite elements interconnecting 252 joints, with 6 degrees of freedom. Figures 4-4 and 4-5 are side view and top view computer-generated plots of this position of the model (steroscopic plots are generated but only right-eye views are presented):

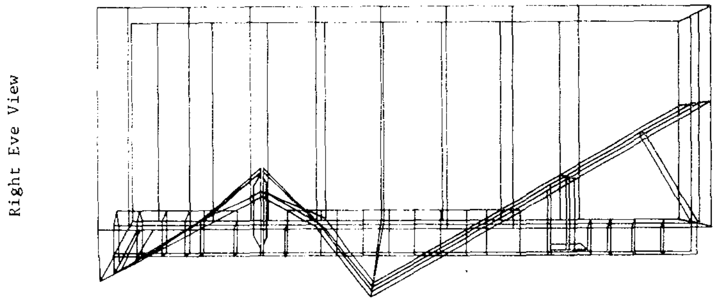

```
Complete B-End Carbody (X=203. to 461.5)HAFCARB Data File (CY=1)
Center of Eyes Location     View Point Location     Roll Angle = 180.0 Deg
  X = 3.31250000E+02          X = 3.31250000E+02    Cone Angle -  20.0 Deg
  Y = -1.00000000E+02         Y = 0.                Eye to Eye =   2.0 Deg
  Z = 5.00000000E+01          Z = 1.58750000E+01
Run No. = HAFCRB            Date = 16SE74
```

Figure 4-4 *Finite Element Model Side View*

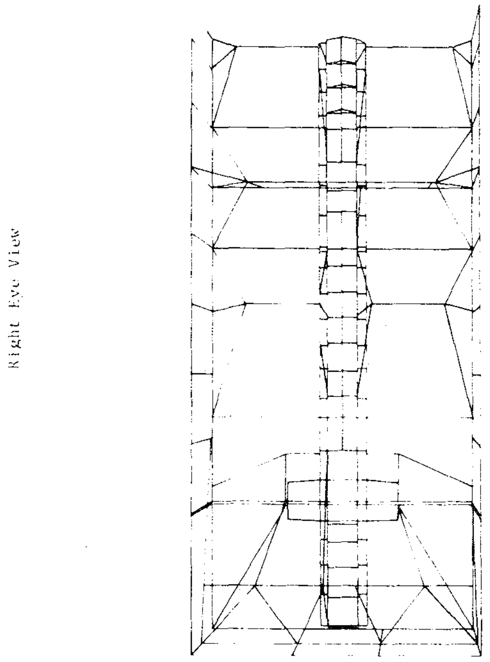

```
Complete B-End Carbody(X=203. to 461-5)HAFCARB Data File(CY=1)
Center of Eyes Location     View Point Location     Roll Angle =  0. Deg
  X = 3.50000000E+02          X = 3.50000000E+02    Cone Angle = 20.0 Deg
  Y = 3.00000000E+01          Y = 3.00000000E+01    Eye to Eye =  2.0 In
  Z = 1.00000000E+03          Z = 1.58750000E+01
Run No. = HAFCRB            Date = 16SE74
```

Figure 4-5 *Finite Element Model Top View*

4.1.3 Finite Element Mass and Stiffness

4.1.3.1 Carbody Stiffness - The initial finite element stiffness model consisted of approximately 3000 degrees of freedom. This size model is too large for economical subsequent calculations. From the analysis standpoint, we are interested in the two or three elastic modes below 10 Hz*. Therefore, in order to achieve a final model with an economic number of degrees of freedom we applied a technique known as Guyan or static reduction. This technique is based on the premise that, over the frequency range of interest, the kinetic energy contribution of many of the degrees of freedom are small. Hence, the motion of these degrees of freedom can be written as a linear combination of a set of retained degrees of freedom. This implies that the reduced or collapsed degrees of freedom are not independent and are not influenced by external forces. Guyan's method permits us to write,

$$\left[\begin{array}{c|c} K_{cc} & K_{cr} \\ \hline K_{rc} & K_{rr} \end{array}\right] \left\{\begin{array}{c} h_c \\ \hline h_r \end{array}\right\} = \left\{\begin{array}{c} 0 \\ F \end{array}\right\} \qquad (4\text{-}2)$$

where the subscripts c and r denote the degrees of freedom of the carbody that are collapsed and retained, respectively.

Equation 4-2 can be partitioned into two sets of equations,

$$\{0\} = \left[K_{cc}\right]\{h_c\} + \left[K_{cr}\right]\{h_r\} \qquad (4\text{-}3)$$

$$\{F\} = \left[K_{rc}\right]\{h_c\} + \left[K_{rr}\right]\{h_r\} \qquad (4\text{-}4)$$

The reduced deflections h_c, can be solved for algebraically from equation 4-3. Hence, we have what is commonly called the reduction transformation,

$$\{h_c\} = -\left[K_{cc}\right]^{-1}\left[K_{cr}\right]\{h_r\} \qquad (4\text{-}5)$$

Substituting the expression for h_c into equation 4-4 we obtain the following results

$$\{F\} = -\left[K_{rc}\right]\left[K_{cc}\right]^{-1}\left[K_{cr}\right]\{h_r\} + \left[K_{rr}\right]\{h_r\} \qquad (4\text{-}6)$$

or

$$\{F\} = \left[\hat{K}\right]\{h_r\} \qquad (4\text{-}7)$$

where $\left[\hat{K}\right] = \left[-K_{rc}\right]\left[K_{cc}\right]^{-1}\left[K_{cr}\right] + \left[K_{rr}\right]$, the reduced stiffness matrix.

The retained degrees of freedom for the reduced half-carbody model include half-body interface degrees of freedom and elected noninterface degrees of freedom suitable for subsequent generation of the carbody mass matrix. The two halves of the carbody were then coupled, i.e., the potential energy of the two halves was added at common interface degrees of freedom. This resulted in a 270 degree-of-freedom stiffness model. Further static reduction was performed on this model, resulting in a 98 degree-of-freedom stiffness model.

4.1.3.2 Carbody Mass - A consistent mass matrix, i.e., the kinetic energy in each finite element, was represented by an approximate velocity distribution consistent with the approximate strain distribution used in the corresponding potential energy, was generated for the half-carbody model. At this point, the mass matrix could have been transformed to the reduced size by use of the combined reduction transformation obtained in the two-stage stiffness reduction. If we write the kinetic energy of the model as

$$KE = 1/2 \left\{\begin{array}{c} \dot{h}_c \\ \dot{h}_r \end{array}\right\}^T \left[\begin{array}{c|c} M_c & \\ \hline & M_r \end{array}\right] \left\{\begin{array}{c} \dot{h}_c \\ \dot{h}_r \end{array}\right\} \qquad (4\text{-}8)$$

---

*Hunting frequencies have been shown to occur at approximately 3 Hz for this type of car.

we see that after substituting equation 4-5 for $\dot{h}_c$, we are required to perform the following large triple product to obtain the kinetic energy expression in terms of the reduced coordinate set,

$$KE = 1/2 \left\{ \dot{h}_r \right\}^T \left[\frac{-\left[K_{cc}\right]^{-1} \left[K_{cr}\right]}{I} \right]^T \begin{bmatrix} M_c & \\ & M_r \end{bmatrix} \left[\frac{-\left[K_{cc}\right]^{-1} \left[K_{cr}\right]}{I} \right] \left\{ \dot{h}_r \right\} \tag{4-9}$$

This triple product was estimated to require excessive computer costs. Therefore, to avoid this cost, a 270 degree-of-freedom total carbody mass matrix was formed directly as a 270 degree-of-freedom finite element representation. The implication here is that while the correct geometry was retained, the definition of the inertia distribution is less precise than could be obtained by the more expensive "consistent" modeling approach.

This mass matrix corresponds to the 270 degree-of-freedom total carbody stiffness matrix described above. Mass contributions of the nonstructural couplers and draft gears were then added. At this point, with the conformable mass and stiffness matrix, the 270 x 98 Guyan reduction transformation was applied to obtain a mass matrix with 98 degrees of freedom corresponding to those retained for the detailed stiffness model discussed earlier.

In addition to the analysis of the empty car as defined by the mass and stiffness properties described above, there was the requirement to analyze the loaded car. To do this, it was necessary to modify the mass properties to account for the lading. Stiffness effects of the coal were assumed negligible. (The model survey of the loaded car, performed after the analysis, indicated this was an erroneous assumption. This point is discussed further at the end of Section 4.1).

The coal (lading) mass was added to the 98 degree-of-freedom mass model through application of a least square technique in which the total coal mass was broken into several discrete lumps, each lump having an assumed six degrees of freedom. To implement the least squares fit technique, we wrote the center of mass motion for each lump in terms of the motion of several adjacent points,

$$\left\{ \dot{h}_A \right\} = \left[T_{cg} \right]_j \left\{ \dot{h}_{cg} \right\}_j \tag{4-10}$$

where

$\left\{ h_A \right\}$ = motion of adjacent degrees of freedom

$\left\{ h_{cg} \right\}_j$ = motion of center of mass of j^{th} lump

$\left[T_{cg} \right]_j$ = rigid body transformation which relates j^{th} cg motion to motion of adjacent points.

The transformation, $\left[T_{cg} \right]$, is rectangular with more rows than columns (there are more degrees of freedom associated with the adjacent points than there are to describe the center of mass motion of the lump cg). A solution for the cg velocities is accommodated by the following operation on equation 4-11,

$$\left[T_{cg} \right]_j^T \left\{ h_A \right\} = \left[T_{cg} \right]_j^T \left[T_{cg} \right]_j \left\{ \dot{h}_{cg} \right\}_j \tag{4-11}$$

which leads to the least squares solution

$$\left\{ \dot{h}_{cg} \right\}_j = \left(\left[T_{cg} \right]_j^T \left[T_{cg} \right]_j \right)^{-1} \left[T_{cg} \right]_j^T \left\{ \dot{h}_A \right\} = \left[T_L \right]_j \left\{ \dot{h}_A \right\} \tag{4-12}$$

for the j^{th} lump cg motion. Now the total kinetic energy of n lumps of lading is

$$KE = \sum_{j=1}^{n} 1/2 \left\{ \dot{h}_{cg} \right\}_j^T \left[M_{cg} \right]_j \left\{ \dot{h}_{cg} \right\}_j \tag{4-13}$$

which, expressed in terms of the adjacent point is

$$KE = \sum_{j=1}^{n} 1/2 \left\{ \dot{h}_A \right\}^T \left[T_L \right]_j^T \left[M_{cg} \right]_j \left[T_L \right]_j \left\{ \dot{h}_A \right\} = \left\{ \dot{h}_A \right\}^T \left[M_A \right] \left\{ \dot{h}_A \right\} \tag{4-14}$$

The mass matrix, $\left[M_A\right]$, expresses the lading mass in terms of the degrees of freedom defined for the empty car.

4.1.3.3 Rigid Body Checks - The nature of finite element modeling is such that there is a great deal of data to be processed and there are only a few "on line" checks available to insure correctness of the results. Two such checking techniques are: Calculation of the structure's total mass properties about some reference point; and for ungrounded structures, obtaining zero strains upon application of rigid body displacements to the stiffness matrix. Both techniques require a rigid body transformation of the model. This transformation relates the displacement for each degree of freedom of the structure to the rigid body displacements of a reference point. This is equivalent to saying each degree of freedom is rigidly linked to the reference point. Symbolically this can be expressed as

$$\left\{h_s\right\} = \left[T_{RB}\right]\left\{h_{ref}\right\} \tag{4-15}$$

where

$\left\{h_s\right\}$ = displacements of structure,

$\left\{h_{ref}\right\}$ = rigid body displacements of reference point, and

$\left[T_{RB}\right]$ = rigid body transformation.

We can use this transformation to obtain the kinetic energy of the structure with respect to the reference point. This will provide us with the mass properties of the structure about the reference point. Recalling the kinetic energy expansion of the car as,

$$KE = 1/2 \left\{\dot{h}\right\}^T \left[M\right] \left\{\dot{h}\right\} \tag{4-16}$$

We can substitute equation 4-15 for the velocities of the structure to arrive at the kinetic energy of the structure with respect to the reference point.

$$KE = 1/2 \left\{\dot{h}_{ref}\right\}^T \left[T_{RB}\right]^T \left[M\right] \left[T_{RB}\right] \left\{\dot{h}_{ref}\right\} \tag{4-17}$$

This resulting 6 x 6 matrix can be checked against the known mass properties of the car to ascertain the accuracy of the model.

To check that we have not accidentally grounded the structure and it is truly free-free, a rigid body displacement of the structure should result in no internal strains of the finite elements representing the model.

A method of applying these rigid displacements to all the degrees of freedom of the structure is obtained through the use of the rigid body transformation. We want

$$\left[K\right] \left\{h_s\right\} = 0 \tag{4-18}$$

But, the structural displacements h_s can be written in terms of the motions of the reference point via equation 4-15. Therefore,

$$\left[K\right] \left[T_{RB}\right] \left\{h_{ref}\right\} = 0 \tag{4-19}$$

Generally, unity displacement of each reference point is assumed, therefore, the product $\left[K\right]\left[T_{RB}\right]$ need only be formed and checked.

4.1.4 Concept of Modal Coordinates

The carbody mass and stiffness models, which have been discussed previously, contain 98 degrees of freedom each. These models, as a result of the reductions, are almost completely coupled, i.e., almost all terms of the matrices are nonzero. Time domain or frequency domain analysis is cumbersome with the model in this form. Furthermore, no explicit frequency information is available to compare to the known frequency regimes of hunting.

Transformation of the carbody model into the normal modes of vibration will produce an uncoupled set of equations in terms of frequencies (eigenvalues) and normal mode shapes (eigenvectors) of the carbody. These mode shapes can be thought of as the spatial distribution of the amplitudes of motion at a natural resonance of the structure. An illustration of this is shown in Figure 4-6. Here we have a tight string that has been plucked in two ways. Application of an initial displacement at the center of the string excites the first resonance. Likewise, by applying equal but opposite displacements at the string's quarter points we are able to excite the second mode or resonant condition. Generally, the excitation is such that several modes are excited simultaneously and the resulting motion is the superposition of all modal amplitudes.

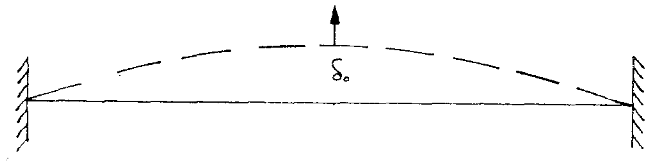

a) First Natural Mode

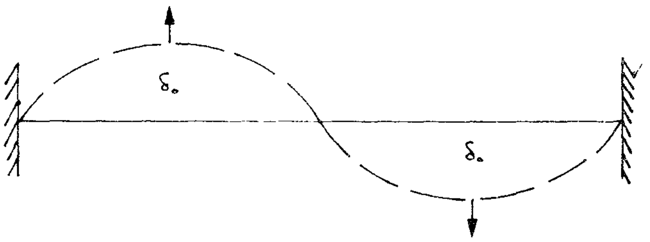

b) Second Natural Mode

Figure 4-6 Illustration of Natural Modes of Vibration

The technique to obtain these normal modes requires the solution of the conservative homogeneous equations of motion for the carbody, as described in Section 3.4.

In addition to computational advantages of analytical modes cited above and in Section 3.4, verification of the model and its imposed assumptions can be obtained by comparing it with a set of test-measured normal modes of vibration of the actual hardware. The analytical model can then be adjusted if discrepancies exist. The test procedure, called a modal survey test, and the model adjustment techniques are discussed next.

4.1.5 Model Correlation of Modal Survey Data

A modal survey test is designed to determine the fundamental modes of vibration of a structure. Recalling the discussion of Figure 4-6 in the preceding section, we saw that by judicious choice of location and phase, i.e., relative signs, of excitation applied to a particular structure (in the case of Figure 4-6, a string) we were able to excite the fundamental vibration modes. This is the underlying principal of a modal survey. The procedure is summarized as follows:

1. The structure is placed on a suitable support, one that is indicative of its service environment. The carbody was placed on air springs at the truck interface. This simulates the car resting atop the truck bolster in normal operation.

2. A preliminary set of excitation forces are selected to excite a particular mode. The forces, applied by electrodynamic shakers, vary both in amplitude and phase with respect to each other. The initial force vectors selected to excite the first torsion, lateral, and vertical bending modes are shown in Figure 4-7.

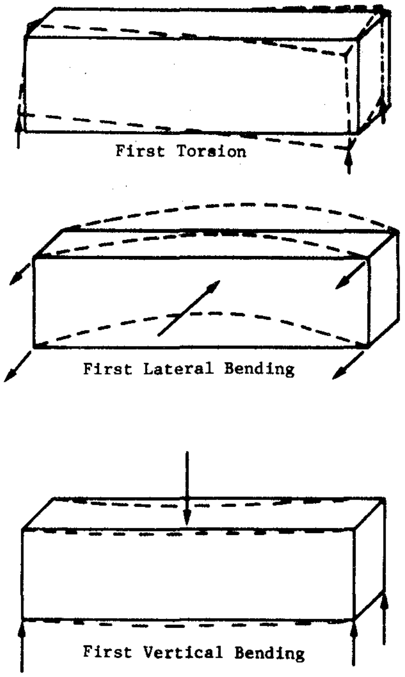

Figure 4-7
Preliminary Force Vector Selected to Excite the First Three Fundamental Modes of the Carbody

3. The electrodynamic shakers are driven sinusoidally over a range of frequencies. This frequency sweep is selected to encompass the natural frequencies of the structure derived from the analytical model.

4. Response, in the form of accelerometer output, is measured. Transfer functions of the accelerometer output to force input are calculated and plotted versus frequency. Additionally, the phase relationship of the accelerometer outputs to the force inputs are determined and plotted. A structural resonant frequency is indicated by the accelerometer output being 90° out of phase (quadratune) with respect to the exciting force. Furthermore, a peak is observed in the imaginary component of the transfer function at the resonant frequency. Figure 4-8 shows this transfer function for the empty carbody 17.64 Hz lateral bending mode.

5. Once the frequency sweep has been completed, the suspected modes are retuned. A frequency dwell is performed at a bandwidth around the suspected modal frequency. The force vector and frequency are adjusted until all responses being measured are 90° out of phase with respect to the force vector.

6. The "purity" of the mode is ascertained by removing the excitation and permitting the response to decay. Beating occurring during decay indicates the presence of other modes. Figure 4-9 presents the decay traces for the lateral bending mode. As can be seen, there is an absence of beating indicating a "pure" mode.

7. Finally, the "pure" mode amplitudes are obtained from the imaginary components of the transfer functions.

The results of the modal survey of the empty and full carbody are shown in Table 4-1. The modes of the carbody moving as a rigid body on the air springs are not used in the hunting analysis but are included here for completeness.

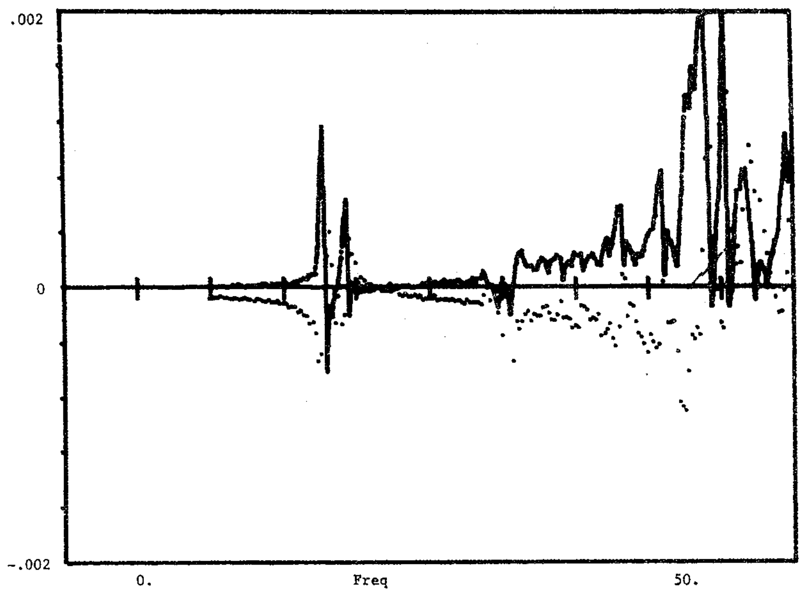

Trk Train 10-24-74 Run 27 WB IMC= .2 Hz
AV1/F8

Figure 4-8 Test Transfer Function Indicating Lateral Bending Mode

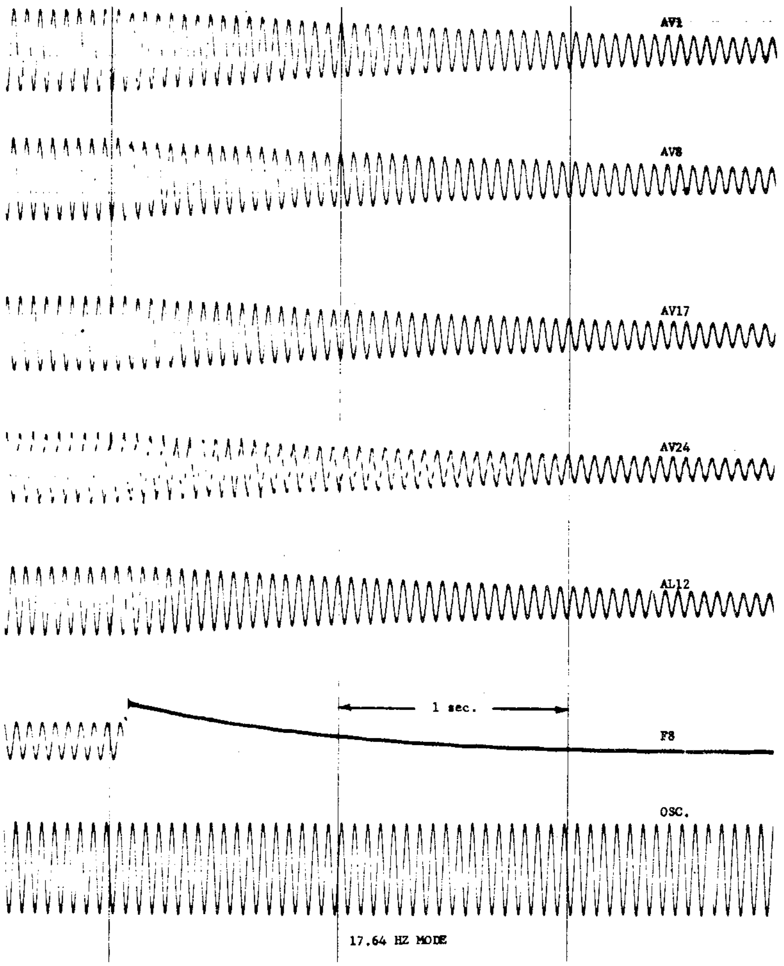

Figure 4-9 Decay Traces of Lateral Bending Mode

Table 4-1 Carbody Modal Survey Results

Empty Frequency (Hz)	Comment	Full Frequency (Hz)	Comment
3.45	Rigid Carbody on Air Springs (Roll)	2.15	Rigid Carbody on Air Springs (Vertical)
6.75	First Torsion Mode	3.3	Rigid Carbody on Air Springs (Roll)
17.64	First Lateral Bending Mode	6.3	First Torsion Mode
29.57	First Vertical Bending Mode	8.85	First Lateral Bending Mode
		14.55	First Vertical Bending Mode

The first torsion mode frequency resides near the suspension frequencies, therefore, it can be expected that significant strain energy of the air springs is reflected in this mode. We desire to have the torsion mode as a true free-free mode and must remove the effects of the air springs. We can write the total stiffness as the sum of the carbody stiffness and air spring stiffness. Thus,

$$\left[K\right] = \left[K_{air}\right] + \left[K_{car}\right] \tag{4-20}$$

If we perform a triple product with the test first torsion mode shape we obtain the following

$$\left\{\phi_T\right\}^T \left[K\right] \left\{\phi_T\right\} = \left\{\phi_T\right\}^T \Big[\left[K_{air}\right] + \left[K_{car}\right]\Big] \left\{\phi_T\right\} = \left\{\phi_T\right\}^T \left[K_{air}\right] \left\{\phi_T\right\} + \left\{\phi_T\right\}^T \left[K_{car}\right] \left\{\phi_T\right\} \tag{4-21}$$

Furthermore, recalling the definition of generalized stiffness, the above can be written as

$$\omega^2 = \omega^2_{air} + \omega^2_{car} \tag{4-22}$$

From this we can obtain the free-free carbody natural frequency. Hence,

$$freq_{car} = \frac{1}{2\pi}\sqrt{\left(2\pi f_{test}\right)^2 - \omega^2_{air}} \tag{4-23}$$

This technique was used with the test modal data. The empty and full free-free torsion frequencies became 5.32 and 4.89 Hz, respectively.

The adjusted test modal data was compared with the analytical results. Table 4-2 shows a comparison of the test and analytical frequencies for the empty car. The analysis is consistently higher in frequency than the test results. However, as shown in Figure 4-10, test and analysis mode shapes compare very well.

Table 4-2 Comparison of Empty Carbody Modal Survey to Analysis

Test (Hz)		Analysis (Hz)	
f = 5.32	Torsion	f = 6.89	Torsion
f = 17.64	Lateral Bending	f = 21.23	Lateral Bending
f = 29.57	Vertical Bending	f = 40.13	Vertical Bending

The frequency discrepancy amounts to approximately 22% for all three modes. This is attributed, in general, to the manner in which the car was built as compared to the drawings which were used as a basis for the finite element model. Two significant factors were noted: (1) lack of planarity of the side walls (the bow in the middle amounted to 2 in.), and (2) lack of continuous welds connecting the sill beam to the car (a continuous weld was assumed in the analysis).

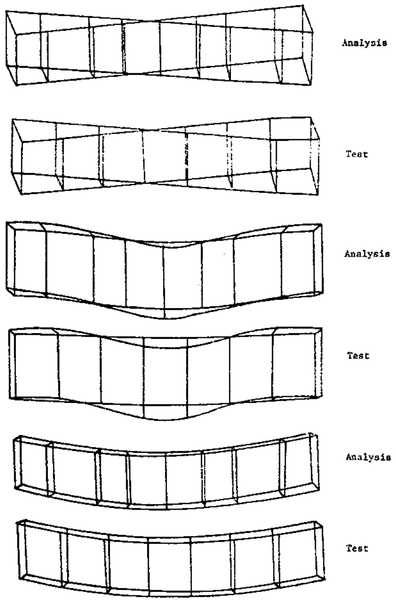

Figure 4-10
Comparison of Analytical and Experimental
Mode Shapes - Empty Car

The analysis data was scaled to more closely match the test results. Referring again to the definition of generalized stiffness, we have for the analysis and test,

$$\begin{aligned} \left\{\phi_A\right\}^T \left[K\right] \left\{\phi_A\right\} &= \omega_A^2 \\ \left\{\phi_T\right\}^T \left[K\right] \left\{\phi_T\right\} &= \omega_T^2 \end{aligned} \qquad (4\text{-}24)$$

Taking the ratio of the analysis to test and rearranging we obtain

$$\left\{\phi_A\right\}^T \left[K\right]\left\{\phi_A\right\} \frac{\omega_T^2}{\omega_A^2} = \omega_T^2 \qquad (4\text{-}25)$$

The analysis stiffness matrix is scaled by the ratio of the test to analysis natural frequencies. Since the error was somewhat uniform, it was decided to use the average of the frequency ratios for the scale factor, i.e.,

$$\text{scale factor} = \frac{1}{3} \sum_{i=1}^{3} \left(f_T/f_A\right)_i^2 = 0.6084.$$

The results of application of this scale factor to the carbody analysis stiffness matrix are shown in Table 4-3.

Table 4-3 Comparison of Scaled Analytical and Experimental Modal Frequencies (Hz)

Mode	Empty Car		
	Analysis		Test
	(Scaled)	(Not Scaled)	
Torsion	5.37	6.89	5.32
Lateral Bending	16.56	21.23	17.64
Vertical Bending	31.30	40.13	29.57

The modal survey test results of the loaded carbody were compared to the analysis of the loaded carbody model. Frequency differences again existed between the test and analysis, as indicated in Table 4-4. The analytical model of the full carbody included the adjustments of the stiffness matrix to match the empty carbody test results. Therefore, it was concluded that the frequency discrepancies could be attributed to the stiffening effects of the coal. The analysis modeled the mass of the coal but assumed the coal added no stiffness. Obtaining an accurate analytical model of the coal would be difficult and require additional empirical data. Although the frequencies of the analysis did not match the test frequencies, the analytical mode shapes showed good correlation to the test mode shapes. Adjustments of the stiffness matrix to match the test results would result in little change to the analytical mode shapes. Therefore, the test frequencies were used along with the analytically derived mode shapes as the model of the full carbody.

Table 4-4 Comparison of Loaded Carbody Modal Survey Frequencies to Analysis Frequencies (Hz)

Mode	Test Frequency	Analysis Frequency
1	4.89	2.81
2	8.80	6.95
3	14.55	16.55

The previous discussions indicate the complexity and difficulty in arriving at a linear model of the structural system. The mating of analysis and test results is required to obtain an accurate engineering model of structure. This test verified analysis approach is further emphasized in the following section on the truck model.

4.2 TRUCK MODEL

4.2.1 Description of Hardware

A typical freight-type is composed of two side frames, two wheel sets, and the bolster connecting the side frames. The carbody weight is supported on a bearing surface of the bolster called the centerplate. Figure 4-11 shows an overview of a typical truck. Structurally, the truck consists of five very stiff members connected with nonlinear joints. There are two basic types of joints: Bolster-side frame and axle-side frame. ASF side control truck joints are shown in Figure 4-12.

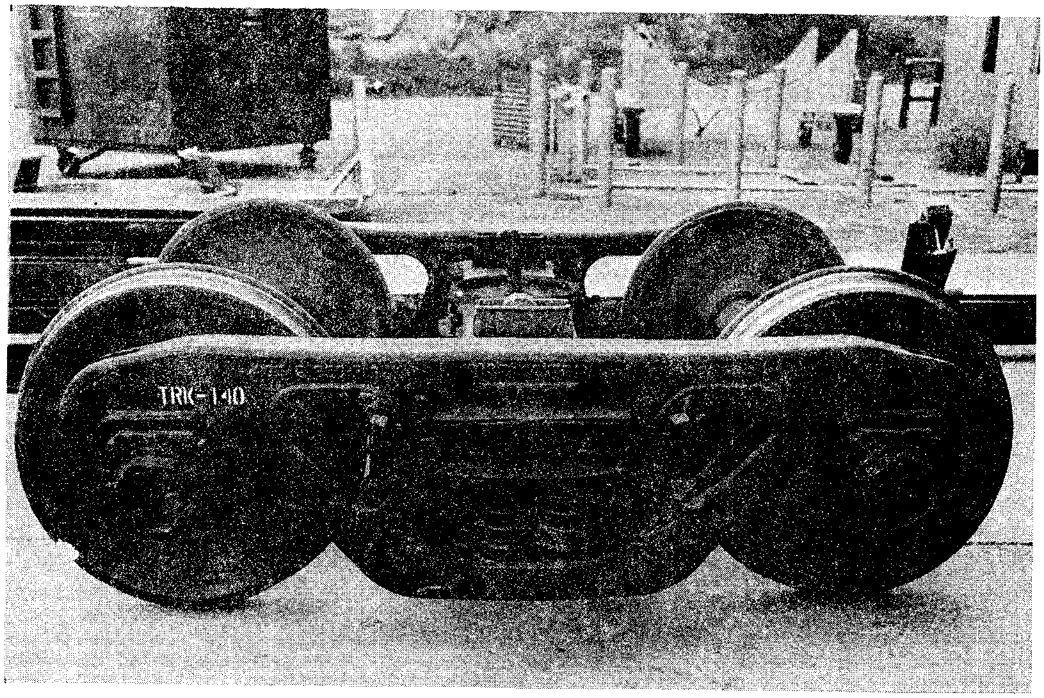

Figure 4-11 Typical Freight Truck

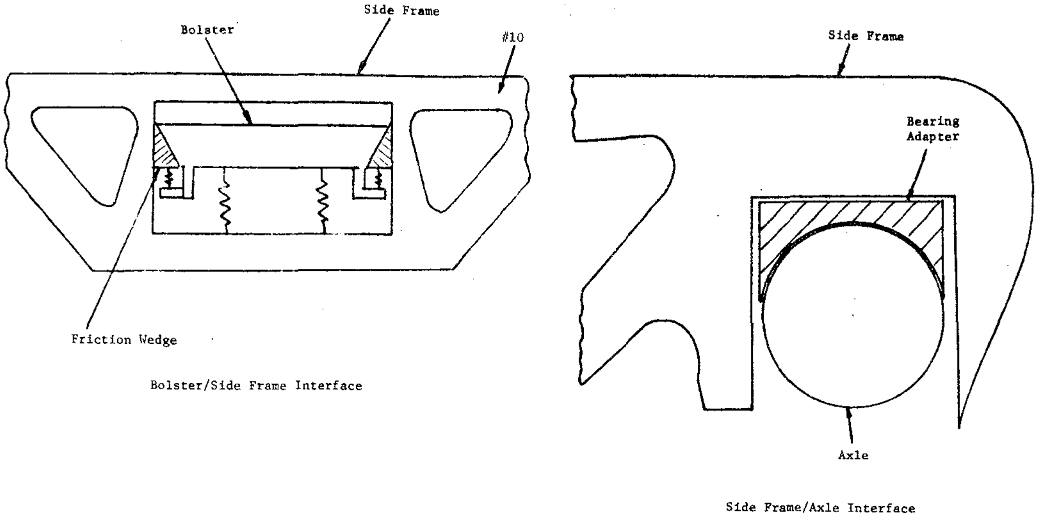

Bolster/Side Frame Interface

Side Frame/Axle Interface

Figure 4-12 ASF Ride Control Truck Joints

The bolster sideframe joints contain two spring groups. The coil spring group supports and and isolates the carbody in vertical and roll type motions. The friction wedge group is a set of springs parallel to the coil group providing preload for the friction wedges. The friction wedges in turn constrain the bolster-side frame relative lateral motions. These joint designs account for the primary differences between truck designs. A comparison of the bolster-side frame designs for ASF and Barber trucks is shown in Figure 4-13. The Barber and ASF designs differ in the manner in which friction is controlled. The force, F_V, (Figure 4-13) is constant for the ASF design and a function of relative vertical displacement between bolster and side frame for the Barber design.

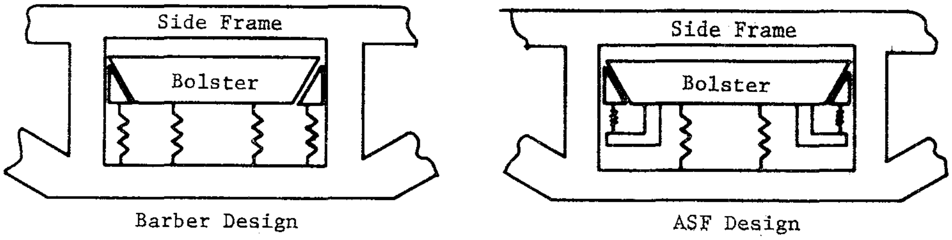

Barber Design

ASF Design

Figure 4-13 Barber and ASF Bolster Side Frame Joint Designs

The axle-side frame joints consist of a bearing adapter that connects the roller bearing to the side frame. The side frame merely rests on top of the bearing adapter. The current designs incorporate tapered bearings that develop frictional forces to oppose the relative lateral, longitudinal, and rotational motions of the axle with respect to the side frame. This design develops high lateral friction forces $\left(\sim 15000_{\text{lb}}\right)$ between the bearings and axles, resulting in a very small lateral displacements of the axles relative to the side frames. Early designs used journal bearings that permitted greater free play in the lateral directions. It will be shown later that the current design aggravated the hunting problem due to this reduced lateral free play.

4.2.2 Preliminary Conceptualization of Truck Model

The preliminary truck model was derived in an analog sense from the physical description of the hardware. The model consisted of five rigid masses connected by massless stiffeners and damping devices at the joints. These model components are sketched in Figure 4-14. The following assumptions were used to arrive at this model:

1. Bolster, sideframes, and axles are rigid, i.e., elastic deflections of these members are small compared to joint motions.

2. There is complete symmetry in the truck, no manufacturing irregularities are considered.

3. Displacements are small enough that geometry changes are negligible, small angle assumptions, etc., apply.

4. Friction in joints is constant coulomb damping, i.e., independent of displacement and its derivatives.

5. There is no coupling between degrees of freedom within a joint, i.e., relative velocity or displacement in one direction of the joint does not result in loads in any other direction of the joint.

6. Motions are small enough so that the bearing adapters remain compressed (vertical motion of the axles relative to the side frames can be neglected).

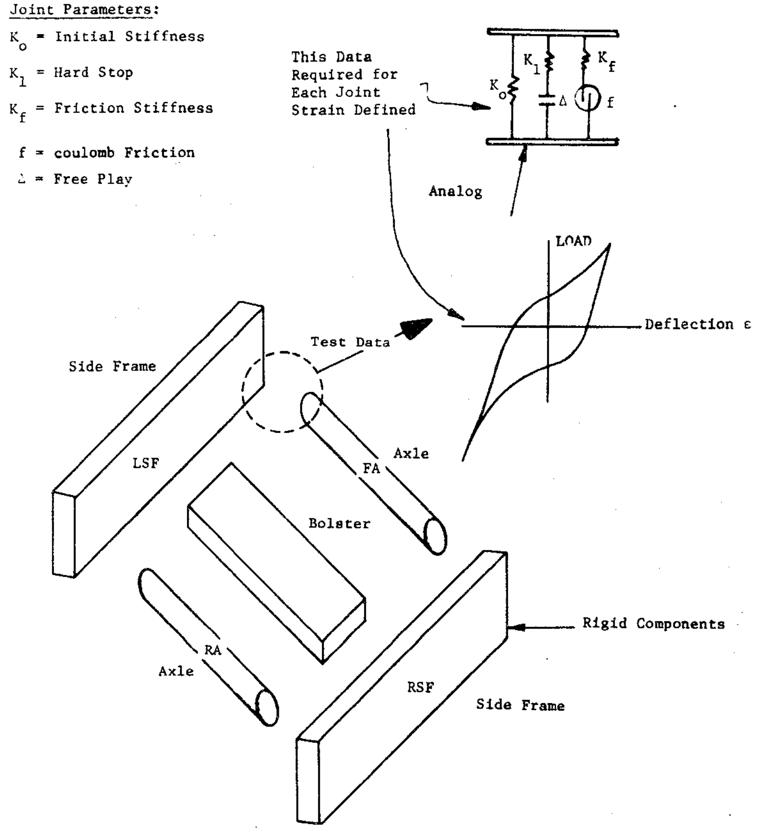

Figure 4-14 Schematic of Modeling Procedure

Strain energy in the joints was first expressed in terms of six rigid body degrees of freedom (dof) at each of two side frames, two axles, and the bolster. This resulted in a 30 degree-of-freedom model of the truck.

The general form of the truck equations of motion was defined by the second row partition of equations 3-31. Application of these equations to the truck model required development of specific j^{th} joint transformation, ψ_j, to describe the strain in the springs of the Figure 4-14 analog in terms of center of gravity motions of the rigid-body masses. Figure 4-15 illustrates the coordinates required for this description at a typical joint.

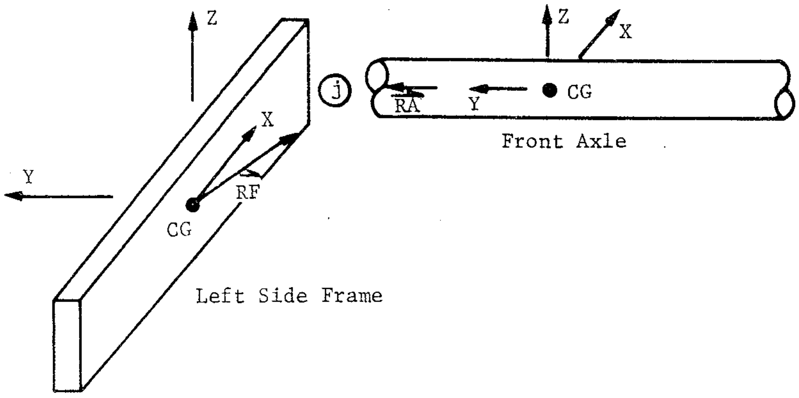

Figure 4-15
CG Coordinate Systems (Typical for Five Rigid Bodies)

The joint displacements expressed in terms of the left side frame cg displacement vector is

$$\vec{h}_{j_{LSF}} = \vec{h}_{LSF} + \vec{\theta}_{LSF} \times \vec{RF} \tag{4-26a}$$

where h includes X, Y, Z, θ_X, θ_Y, θ_Z

and θ includes θ_X, θ_Y, θ_Z

The vector equation, 4-26a, can be expressed in matrix notation as

$$\begin{Bmatrix} X \\ Y \\ Z \\ \theta_X \\ \theta_Y \\ \theta_Z \end{Bmatrix}_{j_{LSF}} = \begin{bmatrix} 1 & & & 0 & L_Z & -L_Y \\ & 1 & & -L_Z & & L_X \\ & & 1 & L_X & -L_X & \\ & & & 1 & & \\ & & & & 1 & \\ & & & & & 1 \end{bmatrix} \begin{Bmatrix} X \\ Y \\ Z \\ \theta_X \\ \theta_Y \\ \theta_Z \end{Bmatrix}_{LSF} \equiv \begin{bmatrix} T \end{bmatrix}_{j_{LSF}} \begin{Bmatrix} h \end{Bmatrix}_{LSF} \equiv \begin{Bmatrix} h \end{Bmatrix}_{j_{LSF}} \tag{4-26b}$$

where L_X, L_Y and L_Z are the respective X, Y, and Z distances from the side frame cg to the joint. A similar transformation can be developed to express the joint displacements in terms of the front axle cg displacement. That is

$$\begin{Bmatrix} h \end{Bmatrix}_{j_{FA}} = \begin{bmatrix} T \end{bmatrix}_{j_{FA}} \begin{Bmatrix} h \end{Bmatrix}_{FA} \tag{4-26c}$$

Therefore, the strains, $\begin{Bmatrix} \varepsilon \end{Bmatrix}_j$, at the joint can be written

$$\begin{Bmatrix} \varepsilon \end{Bmatrix}_j = \begin{Bmatrix} h \end{Bmatrix}_{j_{LSF}} - \begin{Bmatrix} h \end{Bmatrix}_{j_{FA}} = \left[\begin{bmatrix} T \end{bmatrix}_{j_{LSF}} \vdots \begin{bmatrix} T \end{bmatrix}_{j_{FA}} \right] \begin{Bmatrix} h_{LSF} \\ h_{FA} \end{Bmatrix} \equiv \begin{bmatrix} \psi \end{bmatrix}_j \begin{Bmatrix} h \end{Bmatrix} \tag{4-26d}$$

where $\begin{bmatrix} \psi \end{bmatrix}_j$ represents $\begin{bmatrix} T \end{bmatrix}_{jLSF}$ and $\begin{bmatrix} T \end{bmatrix}_{jFA}$ assembled into a matrix that is conformable with the 30 x 1 total truck model displacement vector, $\begin{Bmatrix} h \end{Bmatrix}$. A similar strain transformation, $\begin{bmatrix} \psi \end{bmatrix}_J$, can be developed for every joint. Now the strain dependent forces in each spring of the $J^{\underline{th}}$ joint can be expressed consistent with equation 3-31b, as

$$\begin{Bmatrix} F(\varepsilon) \end{Bmatrix}_j = \begin{bmatrix} K_0 + g(\varepsilon) K_1 \end{bmatrix} \begin{bmatrix} \psi \end{bmatrix}_j \begin{Bmatrix} h \end{Bmatrix} \tag{4-27a}$$

where

$$g(\varepsilon) = \begin{bmatrix} 0 \\ 1 \end{bmatrix} \text{when} \begin{bmatrix} -\Delta > \varepsilon > +\Delta \\ -\Delta < \varepsilon < +\Delta \end{bmatrix} \tag{4-27b}$$

The force in one direction, from equation 4-27, is shown graphically by Figure 4-16. The friction forces at each sliding surface of the $J^{\underline{th}}$ joint can be expressed as,

$$\begin{Bmatrix} F(\dot{\varepsilon},\ d\varepsilon) \end{Bmatrix}_j = \begin{bmatrix} g(\dot{\varepsilon},\ d\varepsilon) \end{bmatrix} \begin{Bmatrix} f \end{Bmatrix}_j \tag{4-28}$$

where $g\left(\dot{\varepsilon},\ d\varepsilon\right)$ is most easily described as the program logic required to track a typical friction force deflection curve as shown in Figure 4-17, rather than as any specific mathematical function. Figure 4-17 depicts a positive constant sliding friction force as long as the time rate of change of joint strain, $\dot{\varepsilon}$, is positive. When the joint comes to rest, that is $\dot{\varepsilon} = 0$, the force is descreased linearly by $-K_f d\varepsilon$. $K_f d\varepsilon$ simulates the static friction force decrease and build up in the reverse direction as the direction of motion reverses. Note that the shape of the curve varies with the operational range of ε. Superposition of Figures 4-16 and 4-17 results in the required total force deflection as described earlier in Figure 4-14.

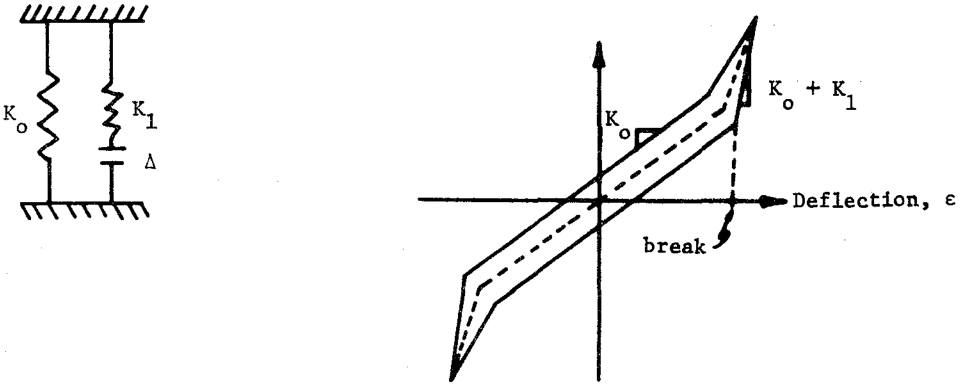

Figure 4-16 Force Deflection Curve for Bottoming-Out-Type Springs

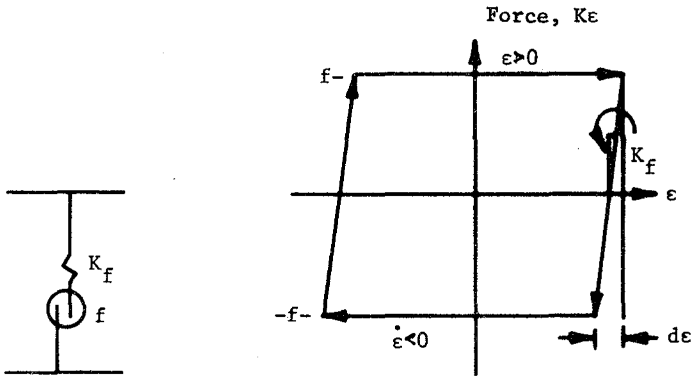

Figure 4-17 Force Deflection Curve for Sliding Friction

All joint spring forces $\left\{F(\varepsilon)\right\}_j$ and joint friction forces $\left\{F\left(\dot{\varepsilon},\ d\varepsilon\right)\right\}_j$ are transformed to the 30 rigid component cg coordinates by the transpose of their corresponding strain transformation $\left[\psi\right]_j^T$ as described earlier in equation 3-30.

4.2.3 Truck Modal Coordinates

The preceding discussion defined the truck model in terms of 30 cg coordinates of the rigid body components. No restriction regarding the type of motion was made. Information supplied by Messers. Cooperrider and Law, and the AAR, indicates that significant motions of the truck can be defined by six principal deflection shapes. Figure 4-18 describes these shapes. (Martin Marietta Corporation test results verify these shapes, as will be discussed in Section 4.2.4). The first two shapes are true rigid-body modes which do not work any of the truck joints. A combination of the third through sixth elastic shape describe all the significant joint motions. Because of the nonlinear joints, normal frequency is meaningless. Therefore, one cannot properly refer to the elastic shapes as modes in the usual sense of the word. However, for ease of writing we will use quotations to refer to the deflection shapes as "modes" in the following development. At this point we should note that these six "modes" do not define any vertical motion of axles or sideframes. Thus, 12 cg coordinates, Z, θ_X and θ_Y for both axles and sideframes, can be deleted (set equal to zero, actually) without imposing any serious constraint on the model. However, weight effects along the Z axis must be considered as will be clarified in the test discussion. Four other coordinates of the original set of 30, i.e., X dof of the bolster and two axles, and θ_Y of the bolster, also can be deleted because they contribute neither significant potential nor kinetic energy in these truck "modes". Therefore, only 14 of the original 30 cg coordinates of the rigid body truck components need be transformed into the "modal" set.

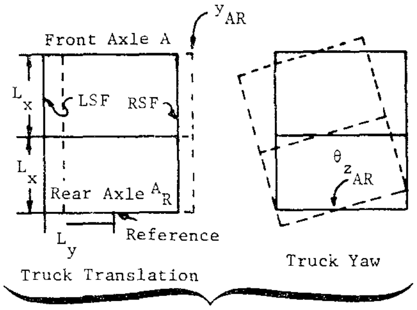

Truck Translation

Truck Yaw

Rigid Body Motion

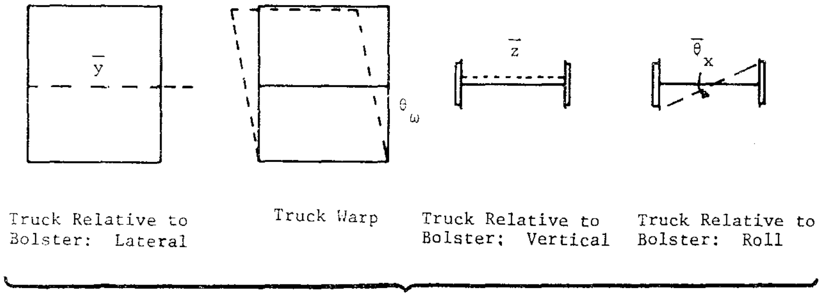

Truck Relative to Bolster: Lateral

Truck Warp

Truck Relative to Bolster; Vertical

Truck Relative to Bolster: Roll

Elastic "Modes"

Figure 4-18 Principal Truck Deflection "Mode" Shapes

Overall, the truck model size was reduced by a factor of five by transforming from the 30 cg coordinates to the six "modal" coordinates described above. The transformation we selected takes the cg of the rear axle as the reference point. Thus, the absolute motion of the remaining 14 cg coordinates was transformed into the absolute motion of the rear axle cg as expressed by the two rigid-body modes, plus motion relative to the rear axle as expressed by the four elastic modes. Referring to Figure 4-18, the transformation from the discrete truck coordinates, $\{h\}_T$, to "modal" truck coordinates, $\{q\}_T$, was written as,

$$\left\{\begin{matrix} \left\{\begin{matrix} Y \\ \theta_Z \end{matrix}\right\}_{AR} \\ \left\{\begin{matrix} \theta_X \\ Y \\ Z \\ \theta_Z \end{matrix}\right\}_{BOL} \\ \left\{\begin{matrix} X \\ Y \\ \theta_Z \end{matrix}\right\}_{RSF} \\ \left\{\begin{matrix} X \\ Y \\ \theta_Z \end{matrix}\right\}_{LSF} \\ \left\{\begin{matrix} Y \\ \theta_Z \end{matrix}\right\}_{AF} \end{matrix}\right\} = \begin{bmatrix} 1 & & & & & \\ & 1 & & & & \\ & & 1 & & & \\ 1 & L_X & & L_X & 1 & \\ & & & & & 1 \\ & 1 & & & & \\ & L_Y & & & & \\ 1 & L_X & & L_X & & \\ & 1 & & 1 & & \\ & -L_Y & & & & \\ 1 & L_X & & L_X & & \\ & 1 & & 1 & & \\ 1 & 2L_X & & 2L_X & & \\ & 1 & & & & \end{bmatrix} \left\{\begin{matrix} Y_{AR} \\ \theta_{ZAR} \\ \bar{\theta}_X \\ \bar{\theta}_\omega \\ \bar{Y} \\ \bar{Z} \end{matrix}\right\} \equiv \left[\phi_T\right] \left\{q_T\right\} \tag{4-29}$$

where the superscript $^{-}$ refers to motion relative to the rear axle cg reference.

Equation 4-29 was then substituted into the second row position of equation 3-31a which was subsequently premultiplied by $\left[\phi_T\right]^T$. If we define the resultant triple matrix product on the truck mass matrix as,

$$\left[\phi_T\right]^T \left[M_T\right] \left[\phi_T\right] \equiv \left[MEQ_T\right] \tag{4-30}$$

the unforced car/truck equations of motion, 3-31a, transform to,

$$\begin{bmatrix} I & \\ & MEQ_T \end{bmatrix} \left\{\begin{matrix} \ddot{q}_c \\ \ddot{q}_T \end{matrix}\right\} + \begin{bmatrix} 2\zeta_c\omega_c & \\ & 0 \end{bmatrix} \left\{\begin{matrix} \dot{q}_c \\ \dot{q}_T \end{matrix}\right\} + \begin{bmatrix} \omega_c^2 & \\ & 0 \end{bmatrix} \left\{\begin{matrix} q_c \\ q_T \end{matrix}\right\} = -\begin{bmatrix} \phi_c^T & \psi_{Ic}^T \\ \phi_T^T & \psi_{IT}^T \end{bmatrix} \begin{bmatrix} & \\ \phi_T^T & \psi_T^T \end{bmatrix} \left(\left\{\begin{matrix} F_I(\varepsilon) \\ F_T(\varepsilon) \end{matrix}\right\} + \left\{\begin{matrix} F_I(\dot{\varepsilon}) \\ F_T(\dot{\varepsilon}) \end{matrix}\right\} \right) \tag{4-31a}$$

As discussed in Section 3, the equations of motion must be solved simultaneously with the nonlinear force equations, 3-31b and 3-31c. These equations also can be transformed to the truck "mode" coordinates. That is,

$$\left\{F(\varepsilon)\right\} = \left[K_\gamma(\varepsilon)\right] \left[\psi\right] \left[\phi_T\right] \left\{q_T\right\} \tag{4-31b}$$

and

$$\left\{F(\dot{\varepsilon})\right\} = \left[K_\gamma(\dot{\varepsilon})\right] \left[\psi\right] \left[\phi_T\right] \left\{\dot{q}_T\right\} \tag{4-31c}$$

4.2.4 Measurement of Truck Model Parameters

The form of equations 4-31 implies that stiffness data, k (ε), and friction data, k $(\dot{\varepsilon})$, need be defined for each $\gamma^{\underline{th}}$ element of the model. Tests to do so would be difficult to devise. The difficulty was avoided by defining "modal" stiffness and friction parameters to replace the individual joint parameters. These new parameters, equivalent to the discrete forces in equation 4-31, were defined as follows:

Let the work done by the discrete stiffness forces be given by,

$$Wk(\varepsilon) = \left\{\varepsilon\right\}^T \left\{F(\varepsilon)\right\} \tag{4-32}$$

Substituting equations 4-26d, 4-29 and 4-31b into 4-32 gives the work as,

$$Wk\left(q_T\right) = \left\{q_T\right\}^T \left[\phi_T\right]^T \left[\psi\right]^T \left[K_\gamma(\varepsilon)\right] \left[\psi\right] \left[\phi_T\right] \left\{q_T\right\} \tag{4-33}$$

Now,

$$\frac{\partial Wk}{\partial \left\{q_T\right\}} \equiv \left\{F\left(q_T\right)\right\} = \left[\phi_T\right]^T \left[\psi\right]^T \left[K_\gamma(\varepsilon)\right] \left[\psi\right] \left[\phi_T\right] \left[q_T\right] = \left[\phi_T\right]^T \left[\psi\right]^T \left\{F_\gamma\left(q_T\right)\right\} = \left[\phi\right]^T \left\{F_{cg}\left(q_T\right)\right\} \tag{4-34}$$

From equation 4-34 we see that the generalized forces on the truck "modes" in equation 4-31a are merely successive transformations of the joint spring forces, $\left\{F_Y(q_T)\right\}$, to discrete coordinate forces, $\left\{F_{CG}(q_T)\right\}$, and finally to modal coordinate forces, $\left\{F(q_T)\right\}$. By substituting $\left[\phi_T\right]^T$ from equation 4-29 into the last form of 4-34, the explicit modal forces can be identified as,

$$\left[\begin{array}{cc|cccc|ccc|ccc|cc}
\text{AR} & & \text{Bolster} & & & & \text{RSF} & & & \text{LSF} & & & \text{AF} & \\
X & \theta_Z & \theta_X & Y & Z & \theta_Z & X & Y & \theta_Z & X & Y & \theta_Z & Y & \theta_Z \\
1 & & & 1 & & & & 1 & & & 1 & & 1 & \\
 & 1 & & L_X & & 1 & L_Y & L_X & 1 & -L_Y & L_X & 1 & 2L_X & 1 \\
 & & 1 & & & & & & & & & & & \\
 & & & L_X & & & & L_X & 1 & & L_X & 1 & 2L_X & \\
 & & & 1 & & & & & & & & & & \\
 & & & & 1 & & & & & & & & &
\end{array}\right]\left\{F_{cg}(q)\right\} = \left\{\begin{array}{ll}
\left.\begin{array}{l} FY_{AR} \\ F\theta_{ZAR} \end{array}\right\}, & \left\{\begin{array}{l} \text{Rigid-body forces} \\ \text{Bolster Plate Friction} \end{array}\right. \\
\overline{F\theta X}, & \text{Bolster Roll Moment} \\
\overline{F\theta\omega}, & \text{Truck Warping Forces} \\
\overline{FY}, & \text{Bolster Lateral Translation Forces} \\
\overline{FZ}, & \text{Bolster Vertical Translation Forces}
\end{array}\right\}$$

Because the truck components are rigid, it is unimportant how the forces are applied provided the resultant forces are as defined above.

For example, any set of forces that result in truck warping will suffice for $\overline{F\theta\omega}$. The resultant $\overline{F\theta\omega}$ can be thought of as the integrated effect of all joint forces associated with the warping mode. Consequently, a good measurement of $\overline{F\theta\omega}$ could be obtained by the test configuration described by Figure 4-19 if there were no friction forces.

Digressing slightly, recall that the development from equations 4-32 through 4-34 considers stiffness forces only. A similar development, with similar results, can be made for friction forces. Therefore, we may define test loads required to overcome both stiffness and friction forces as,

$$\left\{F(q)\right\} = \left[\phi_T\right]^T \left(\left\{F_{cg}(q_T)\right\} + \left\{F_{cg}(\dot{q}_T)\right\}\right) \tag{4-35}$$

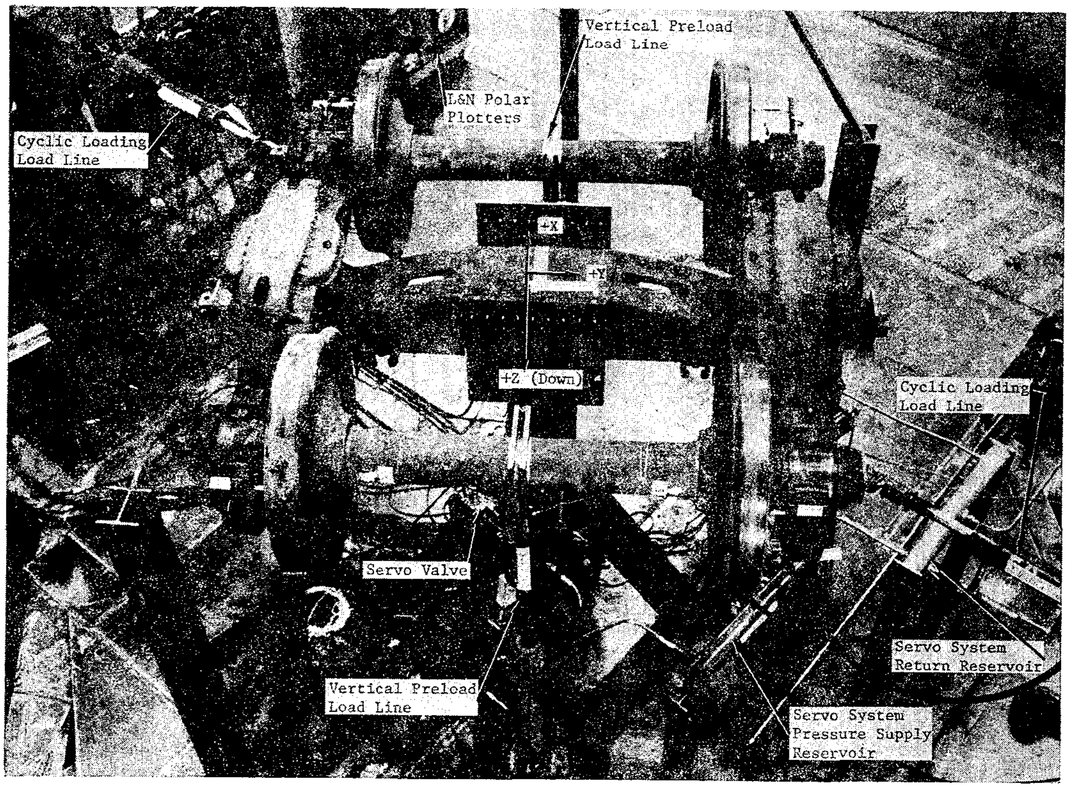

Figure 4-19 Phase Six Setup - Lozenge Mode Racking Loading

A plot of F(q) for the warping (Lozenge) "mode" test data for the loaded car appears as the hysteresis curve shown, along with other examples, in Figure 4-20. As explained earlier, in the discussion of Figures 4-16 and 4-17, the total force deflection relationship, or hysteresis curve, can be synthesized by the superposition of the spring and friction force curves. Inversely, the spring and friction force vs. deflection curves can be synthesized from the measured hysteresis curve. Thus, the analog parameters for the truck "modes", identical in form to K_o, K_1, K_f, f and Δ defined in Figure 4-14 for the joint analog, are empirically derived from test data. Using this analog notation, equation 4-35 can be written as:

$$\left\{F\left(q_T\right)\right\} = \left[K\left(q_T\right)\right] \left\{q_T\right\} + \left[f\left(\dot{q}_T\right)\right] \left\{\dot{q}_T\right\} \qquad (4\text{-}36)$$

where $k_m\left(q_{T_m}\right) q_{T_m}$ gives the instantaneous force on the $m^{\underline{th}}$ nonlinear spring curve (a function of K_{o_m}, K_{1_m} and Δ_m) when the $m^{\underline{th}}$ modal amplitude of a truck is q_{T_m} and $f_m\left(\dot{q}_{T_m}\ \dot{q}_{T_m}\right)$ describes the magnitude and direction of the measured friction force in the $m^{\underline{th}}$ truck mode (a function of K_{f_m}, f_m, and q_{T_m}) when the direction of velocity is given by $\dot{q}_{T_m}$. $k\left(q_T\right)$ and $f\left(\dot{q}_T\right)$ are determined by imposing test forces and boundary conditions on the analytical model, as previously defined, and numerically integrating to determine an analytical truck hysteresis curve. The modal parameters were varied until analytical results correlated with test data. This correlation also is shown in Figure 4-20 for three cases. Table 4-5 lists all of the analog parameters for all truck "modes". Analog parameters for the car-truck interface at the bolster plate also are shown.

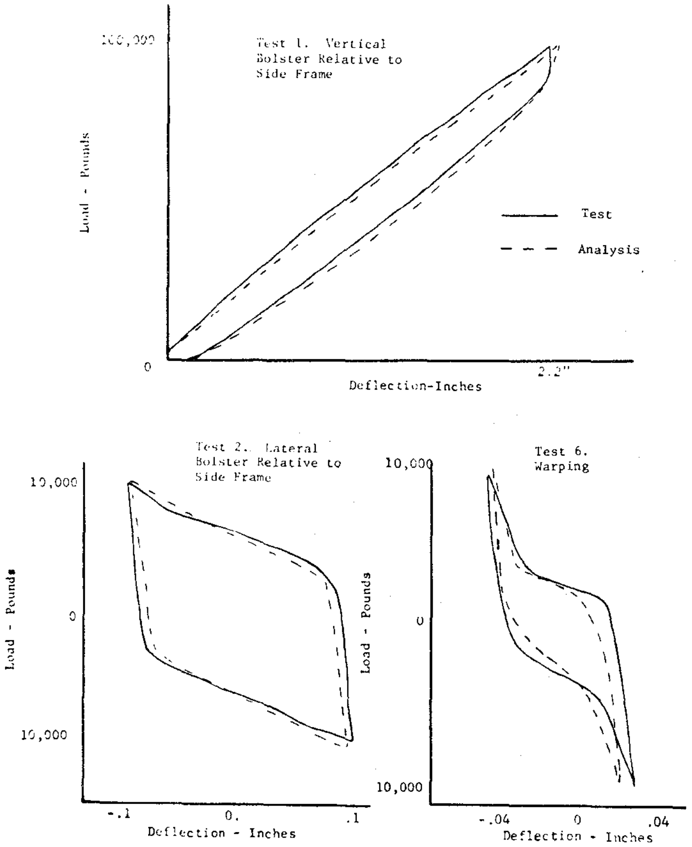

Figure 4-20
Comparison of Analytical and Experimental Hysteresis Results

Table 4-5 Truck Analog Parameters

Location		K_o lb/in [1]	K_1 lb/in [1]	K_f lb/in [1]	f lb [1]	Δ in [1]
Car-truck interface	lateral	0	$(10)^6$	$4.(10)^5$	$2.5(10)^4$	.125
	yaw	0	N/A	$4.(10)^6$	$5.(10)^4$	∞
Bolster:	roll	$6,52(10)^7$	6.52 N/A	$4.(10)^8$	$2.73(10)^5$	∞
Bolster:	vertical	$4.5(10)^4$	N/A	$4.(10)^6$	$7.(10)^3$	∞
Bolster:	lateral	$2.77(10)^4$	$(10)^6$	$4.2(10)^5$	$6.(10)^3$	.5
Truck Wrap		$3.43(10)^7$	$7.(10)^7$	$2.574(10)^8$	$1.4(10)^5$	.00218

(1) See Figures 4-14, 4-16, and 4-17
(2) N/A - Not Applicable

Continuing with the warping (Lozenge) "mode" example, Figure 4-19 shows the test setup devised to measure the total of stiffness and friction force in that "mode". In order to measure Coulomb friction in the joints accurately, the load was applied cyclically while displacement data was recorded continuously. Loading rates of 2 and 4 seconds per cycle were used to determine the relationship, if any, between the measured parameters and velocity. None was detected. Three constant values of vertical bolster load, 20,000, 50,000 and 100,000 pounds, were applied and the warping "mode" test was repeated three times. Thus, three sets of parameters were determined to cover the variations from empty to full loading conditions. Approximately 20 channels of deflection data were recorded. Additional test information can be found in Reference 6.

5.0 THE FORCING FUNCTIONS

Preceding sections discussed the general mathematical concepts, the selection of specific coordinate systems, and the testing required to develop a dynamic model of the unrestrained car/truck system. This section develops mathematical descriptions of the wheel rail interaction forces. It also defines an approach for simulating statistically defined track displacements in time domain analyses, as required for nonlinear system evaluation.

5.1 WHEEL-RAIL INTERACTION FORCES

Figure 5-1 illustrates the wheel set geometry and definitions for the following development of creep forces.

The key to the stability and response characteristics of rail vehicles is the definition of the creep forces acting between the wheel and the rail. These forces are difficult to define, however, a considerable insight to the mathematical problem of stability and response may be gained by a linear treatment of these forces.

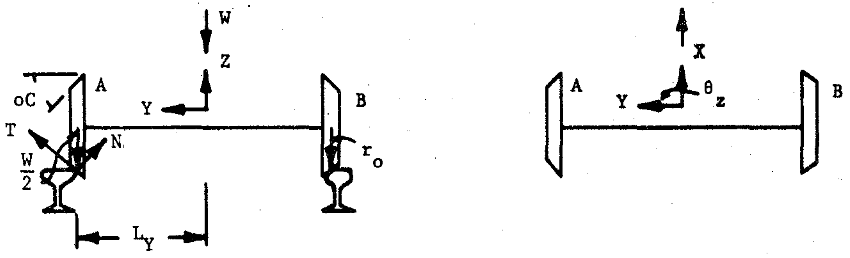

Looking Forward

Looking Down

L_Y = Distance of Contact Point to Wheel Set Center of Mass
N = Normal Force on Wheel Surface
r_o = Nominal Rolling Radius
T = Tangential Force on Wheel Surface
V = Forward Velocity
Y = Lateral Displacement on Wheel Set
α = Conicity or Wheel Taper
θ_Z = Rotation of Wheel Set About Vertical Axis

Figure 5-1 Geometry of Wheel/Rail Interaction

In this linear context, the creep forces, $\left\{F\right\}_c$, are defined to be proportional to the relative velocity between the wheel and rail at the contact point and inversely proportional to the forward velocity, V. That is,

$$\left\{\begin{matrix} F_{AX} \\ F_{AY} \\ F_{BX} \\ F_{BY} \end{matrix}\right\}_C = -\frac{fc}{V}\left\{\begin{matrix} \bar{V}_{AX} \\ \bar{V}_{AY} \\ \bar{V}_{BX} \\ \bar{V}_{BY} \end{matrix}\right\} \qquad (5\text{-}1)$$

The constant of proportionality, f_c, is the so-called "Creep coefficient". We assume the creep coefficient is independent of direction and ignore the spin creep terms. $\bar{V}_{AX}$ is the X velocity of wheel A relative to the rail and F_{AX} is the corresponding wheel rail force. The other forces and velocities have similar meanings.

The following development of relative velocity expressions assumes small motions and hence ignores geometry changes due to these motions.

From Figure 5-1,

$$V_{AX} = 2\pi r\dot{\theta}_Y - L_Y\dot{\theta}_Z \qquad (5\text{-}2)$$

gives the absolute X velocity of wheel A. The radius, r, can be expressed in terms of the nominal rolling radius, r_o, the conicity, α, and the lateral displacement, Y. That is, since

$$r = r_o + \Delta r = r_o\left(1 - \frac{\Delta r}{r_o}\right) \qquad (5\text{-}3)$$

and

$$\Delta r = \bar{Y}_A \tan\alpha \approx \bar{Y}_A\alpha \qquad (5\text{-}4)$$

where $\bar{Y}_A = Y - Y_{t_A}$ is the difference between lateral axle displacement, Y, and lateral displacement of the rail under wheel A, Y_{t_A}. Then

$$V_{AX} = 2\pi r_o \dot{\theta}_Y \left(1 - \frac{\alpha \bar{Y}_A}{r_o}\right) - L_Y \dot{\theta}_Z \tag{5-5}$$

If we define the forward velocity as,

$$V = 2\pi r_o \dot{\theta}_Y \tag{5-6}$$

The X velocity of wheel A relative to the rail becomes,

$$V_{AX} = V - V\left(1 - \frac{\alpha \bar{Y}_A}{r_o}\right) - L_Y \dot{\theta}_Z = -V \frac{\alpha \bar{Y}_A}{r_o} - L_Y \dot{\theta}_Z = -V \frac{\alpha}{r_o} \left(Y - Y\right)_{t_A} - L_Y \dot{\theta}_Z \tag{5-7}$$

A similar development for wheel B gives

$$V_{BY} = V \frac{\alpha}{r_o} \left(Y - Y_{t_B}\right) + L_Y \dot{\theta}_Z \tag{5-8}$$

The Y velocity of wheel A relative to rail A is simply

$$\bar{V}_{AY} = \dot{\bar{Y}} - V\sin\theta_Z \approx \dot{\bar{Y}} - V\theta_Z \tag{5-9}$$

but,

$$\dot{\bar{Y}} = \dot{Y} - \dot{Y}_{tA} = \dot{Y} - V\theta_{ZtA} \tag{5-10}$$

So,

$$\bar{V}_{AY} = \dot{Y} - V\left(\theta_Z + \theta_{ZtA}\right) \tag{5-11}$$

Similarly,

$$\bar{V}_{BY} = \dot{Y} - V\left(\theta_Z + \theta_{ZtB}\right) \tag{5-12}$$

Now equations 5-7, 5-8, 5-11 and 5-12 can be written in matrix form and substituted into 5-1, giving,

$$\begin{aligned}
\begin{Bmatrix} F_{AX} \\ F_{AY} \\ F_{BX} \\ F_{BY} \end{Bmatrix}_C &= \frac{-fc}{v}\left(\begin{bmatrix} \frac{-V\alpha}{r_o} & \\ & -V \\ \frac{V\alpha}{r_o} & \\ & -V \end{bmatrix} \begin{Bmatrix} Y \\ \theta_Z \end{Bmatrix} + \begin{bmatrix} & -L_Y \\ 1 & \\ & L_Y \\ 1 & \end{bmatrix} \begin{Bmatrix} \dot{Y} \\ \dot{\theta}_Z \end{Bmatrix} + \begin{bmatrix} \frac{V\alpha}{r_o} & & & \\ & -V & & \\ & & \frac{-V\alpha}{r_o} & \\ & & & -V \end{bmatrix} \begin{Bmatrix} Y_{tA} \\ \theta_{ZtA} \\ Y_{tB} \\ \theta_{ZtB} \end{Bmatrix} \right) \\
&= -f_c \begin{bmatrix} \frac{\dot{\alpha}}{r_o} & \\ & -1 \\ \frac{\alpha}{r_o} & \\ & -1 \end{bmatrix} \begin{Bmatrix} Y \\ \theta_Z \end{Bmatrix} - \frac{fc}{V} \begin{bmatrix} & -L_Y \\ 1 & \\ & -L_Y \\ 1 & \end{bmatrix} \begin{Bmatrix} \dot{Y} \\ \dot{\theta}_Z \end{Bmatrix} - fc \begin{bmatrix} \frac{\alpha}{r_o} & & & \\ & -1 & & \\ & & \frac{-\alpha}{r_o} & \\ & & & -1 \end{bmatrix} \begin{Bmatrix} Y_{tA} \\ \theta_{ZtA} \\ Y_{tB} \\ \theta_{ZtB} \end{Bmatrix}
\end{aligned} \tag{5-13}$$

Equation 5-13 applies to both the front and rear axles of a truck. However, our model does not contain coordinates of each wheel at which to apply the wheel rail creep forces as developed.

Also, the axle cg coordinates have been transformed to the truck "modes" as described in equation 4-29. To remedy these situations we can write the first two rows (corresponding to the rear axle) and last two rows (corresponding to the front axle) of equation 4-29 as,

$$\begin{Bmatrix} \begin{Bmatrix} Y \\ \theta_Z \end{Bmatrix}_{AR} \\ \begin{Bmatrix} Y \\ \theta_Z \end{Bmatrix}_{AF} \end{Bmatrix} = \left[\begin{array}{ccc} 1 & & \\ & 1 & \\ \hline 1 & 2L_X & 2L_X \\ & 1 & \end{array}\right] \begin{Bmatrix} Y_{AR} \\ \theta_{ZAR} \\ \theta_{\omega} \end{Bmatrix} \tag{5-14}$$

Equation 5-14 can be used to generate dof at all wheels on which to apply the wheel rail forces by,

$$\left\{\begin{matrix}\left\{\begin{matrix}X_A\\Y_A\\X_B\\Y_B\end{matrix}\right\}_{AR}\\\left\{\begin{matrix}X_A\\Y_A\\X_B\\Y_B\end{matrix}\right\}_{AF}\end{matrix}\right\} = \left[\begin{array}{cc|cc} & -L_Y & & \\ 1 & & & \\ & L_Y & & \\ 1 & & & \\ \hline & & & -L_Y \\ & & 1 & \\ & & & L_Y \\ & & 1 & \end{array}\right] \left[\begin{array}{ccc} 1 & & \\ & 1 & \\ \hline 1 & 2X & 2X \\ & 1 & \end{array}\right] \left\{\begin{matrix}Y_{AR}\\\theta_{ZAR}\\\overline{\theta}_\omega\end{matrix}\right\} = \left[\begin{array}{ccc} & L_Y & \\ 1 & & \\ & L_Y & \\ 1 & & \\ \hline & -L_Y & \\ 1 & 2L_X & 2L_X \\ & L_Y & \\ 1 & 2L_X & 2L_X \end{array}\right] \left\{\begin{matrix}Y_{AR}\\\theta_{ZAR}\\\overline{\theta}_\omega\end{matrix}\right\} \tag{5-15}$$

Now equations 5-13, 5-14, and 5-15 can be used to write the work done by the wheel-rail creep forces in the truck mode coordinates. The partial derivative of that work expression with respect to the truck "mode" coordinates yields the forces moving in those coordinates.

That is, the creep forces $\{F\}_c$, are

$$\left\{\begin{matrix}F_{YAR}\\F\theta_{ZAR}\\F\theta_\omega\end{matrix}\right\}_C = -\begin{bmatrix} & 1 & & 1 & & 1 & & 1 \\ -L_Y & & L_Y & & -L_Y & 2L_X & L_Y & 2L_X \\ & & & & & 2L_X & & 2L_X \end{bmatrix} \left(fc \begin{bmatrix} \frac{-\alpha}{r_o} & & & \\ & -1 & & \\ \frac{\alpha}{r_o} & & & \\ & -1 & & \\ & & \frac{\alpha}{r_o} & \\ & & & -1 \\ & & \frac{\alpha}{r_o} & \\ & & & -1 \end{bmatrix} \begin{bmatrix} 1 & & \\ & 1 & \\ 1 & 2L_X & 2L_X \\ & 1 & \end{bmatrix} \left\{\begin{matrix}Y_{AR}\\\theta_{ZAR}\\\overline{\theta}_\omega\end{matrix}\right\} \right.$$

$$\left. + \frac{fc}{V} \begin{bmatrix} & -L_X & & \\ 1 & & & \\ & L_Y & & \\ 1 & & & \\ & & & -L_Y \\ & & 1 & \\ & & & L_Y \\ & & 1 & \end{bmatrix} \begin{bmatrix} 1 & & \\ & 1 & \\ 1 & 2L_X & 2L_X \\ & 1 & \end{bmatrix} \left\{\begin{matrix}\dot{Y}_{AR}\\\dot{\theta}_{ZAR}\\\dot{\overline{\theta}}_\omega\end{matrix}\right\} + fc \left[\begin{array}{cccc|cccc} \frac{-\alpha}{r_o} & & & & & & & \\ & -1 & & & & & & \\ & & \frac{\alpha}{r_o} & & & & & \\ & & & -1 & & & & \\ \hline & & & & \frac{\alpha}{r_o} & & & \\ & & & & & -1 & & \\ & & & & & & \frac{\alpha}{r_o} & \\ & & & & & & & -1 \end{array}\right] \left\{\begin{matrix}\left\{\begin{matrix}Y_{tA}\\\theta_{ZtA}\\Y_{tB}\\\theta_{ZtB}\end{matrix}\right\}_{AR}\\\left\{\begin{matrix}Y_{tA}\\\theta_{ZtA}\\Y_{tB}\\\theta_{ZtB}\end{matrix}\right\}_{AF}\end{matrix}\right\} \right)$$

$$\equiv -\left[KC\right]\left\{q_T\right\} - \left[DC\right]\left\{\dot{q}_T\right\} - \left[KTC\right]\left\{h_T\right\} \tag{5-16}$$

These forces are developed for both trucks. Note that only three of the truck modes, Y_{AR}, $\theta\ Z_{AR}$, and $\overline{\theta}_\omega$, "feel" these wheel-rail forces. Also, creep forces contribute stiffness (displacement dependent terms) and damping (velocity dependent terms) to the affected "modes". These are the terms which determine the "hunting" stability of the system.

In addition to the above creep forces, gravity and wheel conicity combine to produce a lateral force. Figure 5-2 illustrates the wheel set geometry and basic equations for the wheel-rail gravity forces. The force and displacement are expressed, in Figure 5-2, in an axle cg coordinate system. Again, the force and displacement must be transformed from the axle c.g. to the truck "modal" coordinates. This is done by using rows one and three of Equation 5-14 in conjunction with the equation for Fy in Figure 5-2 to develop the work expression, and subsequentially taking the partial derivative with respect to the "modal" coordinates as before, to obtain the modal forces. That is, the gravity forces, $\{F\}_G$, are

$$\begin{Bmatrix} F_{AR} \\ F\theta_{ZAR} \\ F_{\overline{\theta\omega}} \end{Bmatrix} = F_Y \begin{bmatrix} 1 & 1 \\ & 2L_X \\ & 2L_X \end{bmatrix} \begin{bmatrix} 1 & & \\ 1 & 2L_X & 2L_X \end{bmatrix} \begin{Bmatrix} Y_{AR} \\ \theta_{ZAR} \\ \overline{\theta}_\omega \end{Bmatrix} = -\frac{F_{n\alpha}}{L_Y} \begin{bmatrix} 2 & 2L_X & 2L_X \\ 2L_X & 4L_{X^2} & 4L_{X^2} \\ 2L_X & 4L_{X^2} & 4L_{X^2} \end{bmatrix} \begin{Bmatrix} Y_{AR} \\ \overline{\theta}_{ZAR} \\ \overline{\theta}_\omega \end{Bmatrix} = \left[KG\right] \left\{q_T\right\} \tag{5-17}$$

These gravity forces also are developed for both trucks.

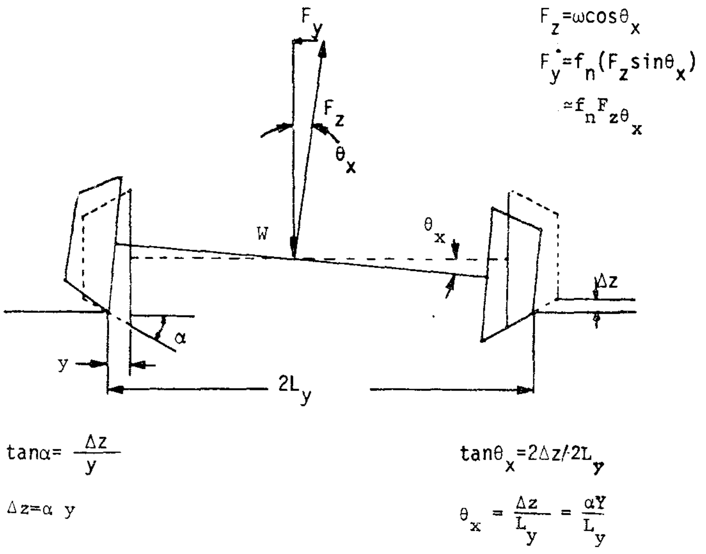

$F_z = \omega\cos\theta_x$

$F_y = f_n(F_z\sin\theta_x)$

$\approx f_n F_z \theta_x$

$\tan\alpha = \frac{\Delta z}{y}$

$\Delta z = \alpha\ y$

$\tan\theta_x = 2\Delta z/2L_y$

$\theta_x = \frac{\Delta z}{L_y} = \frac{\alpha Y}{L_y}$

where f_n = lateral wheel friction coefficient

$F_n = f_n W$, maximum lateral friction reaction to weight (total 2 wheel **reaction**)

Figure 5-2 Geometry for Gravity Spring

5.2 GENERATION OF RAIL DISPLACEMENT TIME HISTORY

In the preceding paragraphs rail displacement dependent forces were defined (Equation 5-13). The development assumed that rail irregularities are known as a function of distance along the track. When such is the case, rail irregularities as a function of time can be determined for a given train speed.

However, rail irregularity data, although measured as a function of time and/or distance traveled, generally are cast in statistical form to facilitate interpretation and storage. That is, condition of a length of track can be evaluated by comparing the measured deviation of rail irregularity from a zero mean with some acceptable deviation value. An example of statistical track data is shown in Figure 5-3 in the form of a probability distribution chart for measured track centerline irregularities. Figure 5-3 also illustrates how the distribution chart is generated from the measured time or spatial data. For clarity, the illustration depicts a very short length of track, but the power of the distribution chart to summarize and store many miles of track data is evident.

Unfortunately, probability distribution data is not unique. It does not describe the frequency content of the track. Spectral analysis is required to determine this track characteristic. The result of spectral analysis is Power Spectral Density (PSD), which is the intensity of rail irregularities described as a function of frequency. An example of power spectral density data is shown in Figure 5-4. Measured track centerline irregularities, the same as used to obtain the

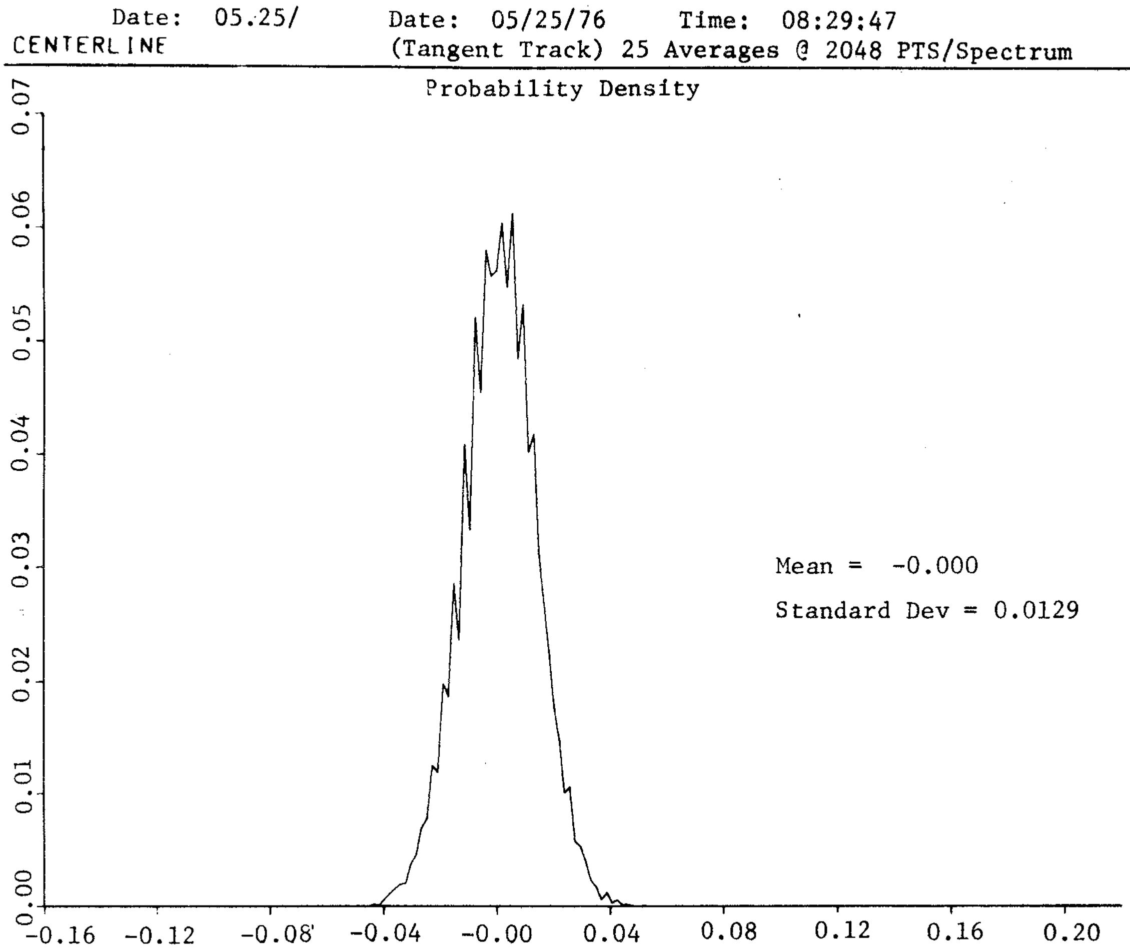

(a) Lateral Displacement of Track Centerline

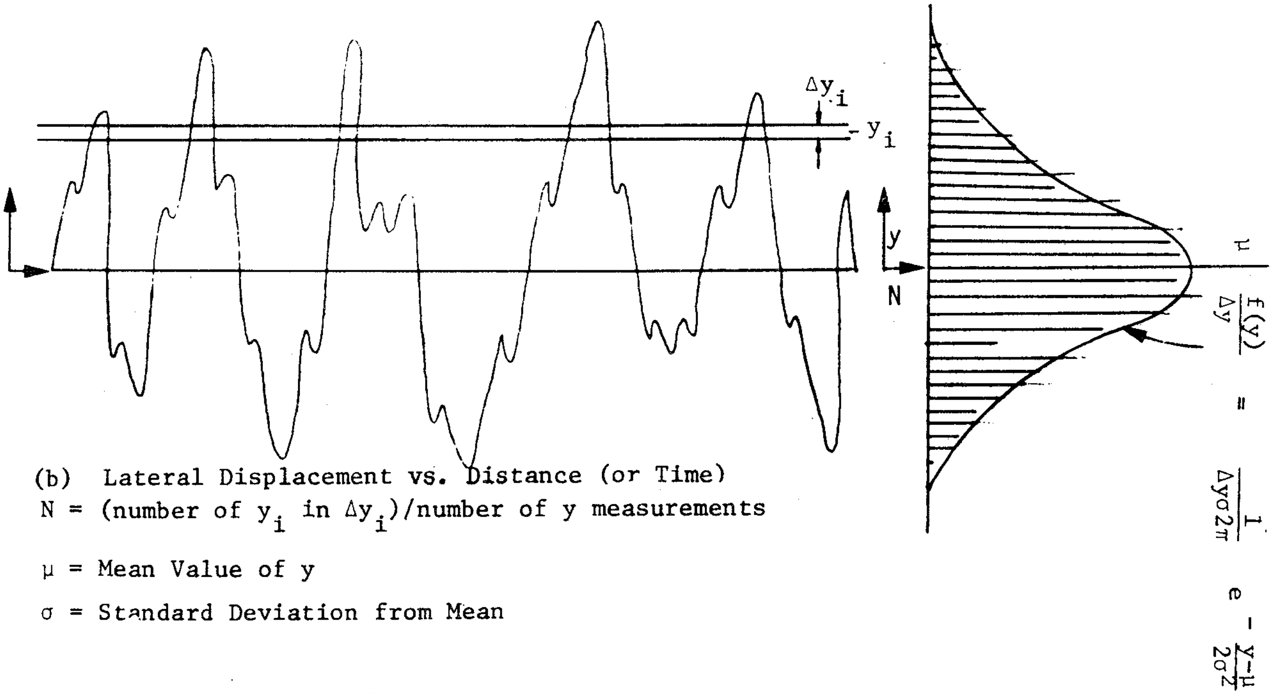

(b) Lateral Displacement vs. Distance (or Time)

N = (number of y_i in Δy_i)/number of y measurements

μ = Mean Value of y

σ = Standard Deviation from Mean

Figure 5-3 Statistical Summarization of Data.

probability density chart in Figure 5-3, were analyzed to obtain this spectrum. The example data, shown in terms of spatial frequency, can be converted to cycles per unit time as would be experienced at a given speed. The integral of the PSD over the frequency range is equivalent to the variance obtained from the probability distribution approach to data summarization. Thus, the square root of this integral, called the root mean squared (rms) value, is equal to the deviation.

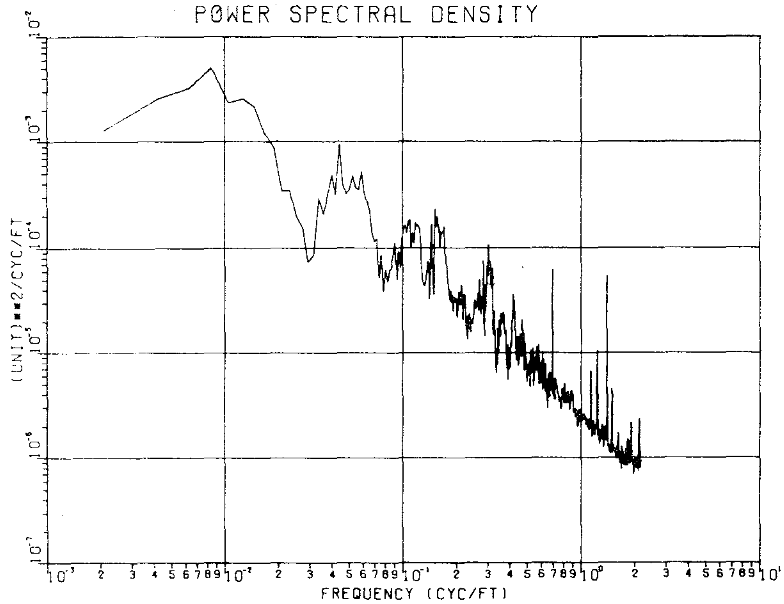

Figure 5-4 Spectral Summarization of Data

If the truck could be represented by a linear mathematical model, the PSD of rail irregularity data would be sufficient to calculate PSD of a car-truck analytical model response. Integration of this response PSD over the frequency range would yield an analytical rms response value. This could be compared with the rms of measured response data obtained during testing on the same length of track over which the rail irregularities were measured. Such a comparison would establish the validity of the linear mathematical model.

However, when model nonlinearities are significant, only time domain response analyses will suffice. That is, a time history (or a spatial distribution) of measured rail irregularities must be applied to force the model. At first glance, this would imply that corresponding time histories of measured response data must be available with which to compare experimental and theoretical results. This approach is not viable because rail irregularities and vehicle responses were not measured simultaneously. We avoid this dilemma by generating a time history of rail irregularities consistent with available rail probability distribution and PSD data. The calculated responses from the synthesized rail description is then spectrally analyzed, as described above for a linear analysis, to obtain rms numbers to compare with the rms from the PSD of measured data from model verification. (Or, a comparison of statistically summarized test and analysis results could be used.)

Our approach to obtain the desired time history is to generate a Fourier Series where the Fourier coefficients, A_n and B_n, are obtained from rail irregularity PSD data and the phase, θ_n, between each term is randomly selected. That is,

$$Y(t) = \sum_{n=1}^{N} \left(A_n \sin \omega_n t + B_n \cos \omega_n t\right) \qquad (5\text{-}18)$$

Where

$$A_n = \sqrt{PSD_n \cdot X\Delta\omega_n} \;\sin\theta_n \qquad (5\text{-}19)$$

and,

$$B_n = \sqrt{PSD_n \cdot X\Delta\omega_n} \;\cos\theta_n \qquad (5\text{-}20)$$

A specific result for centerline irregularities is shown in Figure 5-5. This spatial distribution was generated by selecting PSD values from Figure 5-4 at .002 intervals on the abscissa, or spatial frequency scale. 800 terms were input to the series of equation 5-18 in this manner. A random number generator was used to select numbers between 0 and 1 to determine

$$\theta_n = 2\pi R_n \text{ where } 0 \le R_n \le 1 \qquad (5\text{-}21)$$

A statistical analysis of the generated centerline irregularities was conducted to determine the deviation, or RMS value. The curve was then scaled by the ratio of the test deviation value (Figure 5-3a) over our calculated value. Figure 5-5 reflects this scaling. (Note that the standard deviation shown in Figure 5-5 is .088 inches whereas Figure 5-3a shows a .0129 inch standard deviation. .088 inches is the correct value for centerline alignment as identified on page 5 of reference 7.) A spectral analysis of Figure 5-5 result was conducted to assure that the test frequency content was retained.

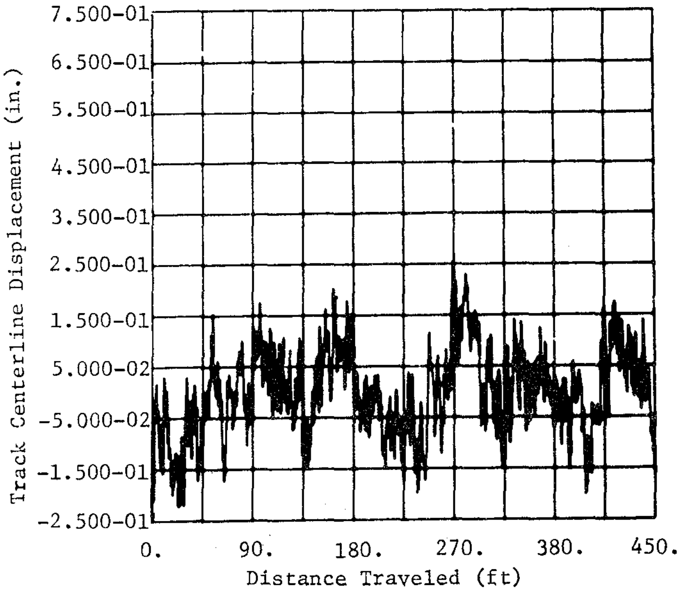

Figure 5-5 Track Centerline Displacement vs Track Distance

6.0 COUPLED SYSTEM EVALUATION

The general equations of motion were developed in Section 3. These equations were transformed to specific modal coordinates of the carbody and truck in Section 4. Then, wheel-rail interactions were developed and transformed to the modal coordinates in Section 5. In this section, the coupled modal equations of motion are restated with explicit statement of all coupling and excitation forces. An example of nonlinear system response to simulated track irregularities is presented.

6.1 COUPLED EQUATIONS OF MOTION

When the notations of equations 4-11, 5-13, and 5-17 are adopted, the coupled carbody-truck equations of motion and nonlinear force equations appear as,

$$\begin{bmatrix} I & & \\ & M_{EQ_{Tf}} & \\ & & M_{EQ_{TR}} \end{bmatrix} \begin{Bmatrix} \ddot{q}_c \\ \ddot{q}_{TF} \\ \ddot{q}_{TR} \end{Bmatrix} + \begin{bmatrix} 2\zeta_c\omega_c & & \\ & 0 & \\ & & 0 \end{bmatrix} \begin{Bmatrix} \dot{q}_c \\ \dot{q}_{TF} \\ \dot{q}_{TR} \end{Bmatrix} + \begin{bmatrix} \omega_c{}^2 & 0 & 0 \end{bmatrix} \begin{Bmatrix} q_e \\ q_{TF} \\ q_{TR} \end{Bmatrix} = \begin{bmatrix} \phi_{CF}^T & \phi_{CR}^T \\ I & \\ & I \end{bmatrix} \left(\begin{Bmatrix} F(q_{TF}) \\ F(q_{TR}) \end{Bmatrix} + \begin{Bmatrix} F(\dot{q}_{TF}) \\ F(\dot{q}_{TR}) \end{Bmatrix} + \begin{Bmatrix} F_{tF} \\ F_{tR} \end{Bmatrix} \right) \qquad (6\text{-}1a)$$

$$\{F(q_T)\} = \left(-\left[k(q_T)\right] - [KC] - [KG]\right)\{q_T\} - \left[k_B(q_c - q_T)\right][\phi_c]\{q_c\} \qquad (6\text{-}1b)$$

$$\{F(\dot{q}_T)\} = \left(-\left[f(q_T)\right] - [DC]\right)\{q_T\} - \left[f_B(\dot{q}_c - \dot{q}_T)\right][\phi_c]\{\dot{q}_c\} \qquad (6\text{-}1c)$$

$$\{F_T\} = -[KTC]\{h_T\} \qquad (6\text{-}1d)$$

Equations 6-1b through 6-1d exist for both trucks. The bolster terms, k_B and f_B, have been explicitly identified in Equation 6-1 to emphasize the coupling that exists between the car modes, q_c, and truck "modes", q_T. This coupling was alluded to in the definition of bolster plate analog parameters given in Table 1. The modeling assumption in this area is that the carbody and bolster plate remain in contact at all times.

An approach toward verification of the system model, as described by equation 6-1, was required. Rail geometric irregularities were measured on some length of operational track and the response of the 80-ton hopper car rolling on that track was measured. These rail irregularities were applied to the model and the analytical responses were compared with test data. The following paragraphs describe this verification effort.

6.2 RESPONSE TO RAIL IRREGULARITIES

A considerable amount of operational testing with the 80-ton Hopper Car has been completed. Both rail irregularities and car responses have been recorded. Measured centerline irregularity data was analytically simulated, as discussed in Section 5, and used as the h_T vector in equation 6-1d to excite the nonlinear model. The spatial distribution of centerline irregularity, Figure 5-5, was multiplied by a forward velocity to obtain the required time history. Three forward velocities were analyzed: 60 fps (40.9 mph), 80 fps (54.5 mph), and 100 fps (68 mph). Each analysis was run for eight seconds. The motion of all model coordinates was predicted by these analyses. Lateral wheel/rail forces and motion relative to the rail at the front axle of the front truck also were predicted by these analyses and are presented in Figures 6-1 through 6-6. RMS values over the eight-second sample were calculated for each result. These are included in the respective figures. Figure 6-7 presents measured front truck cg lateral displacements relative to the rail, as a function of time, for three freight car dynamics field test conditions. These conditions were chosen because they correspond closely to the three analyzed conditions identified above. As mentioned in Section 5-2, no direct time comparison is possible because the time relationship is lost in the statistical methods of handling test data. However, quantitative comparisons can be made between analysis and test by superimposing peak and RMS values from analysis on the test data. Figure 6-7 provides this form of analytical results. Although the extent of this comparison is limited, these results show that the model predicts motions within the order of magnitude observed in test. Two further steps can be taken to improve the quality of comparison:

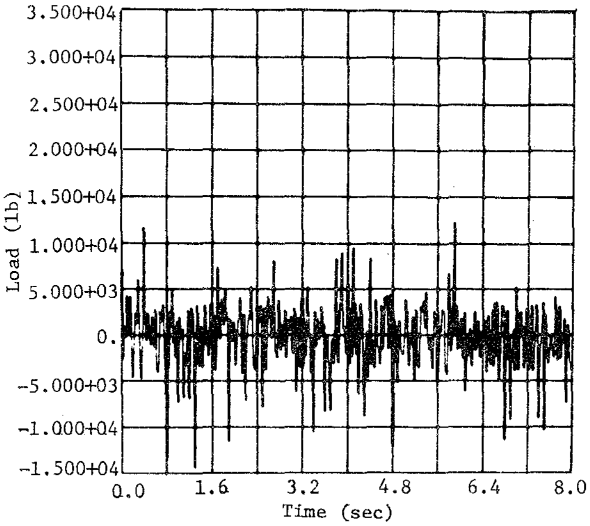

Figure 6-1 Front Truck, Front Axle Wheel/Rail Lateral Force vs. Time (40.9 mph)

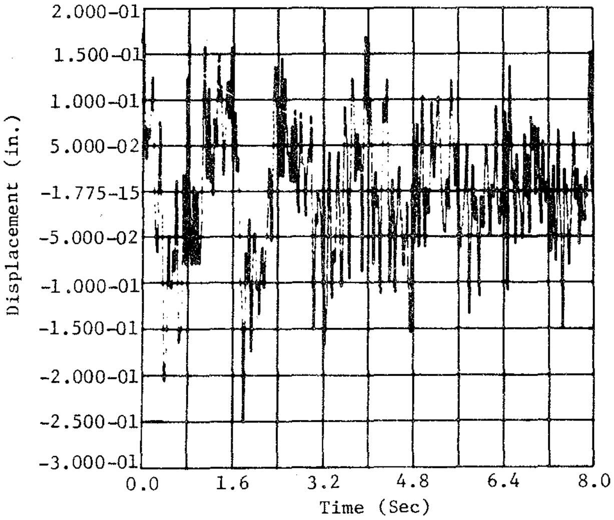

Figure 6-2 Front Truck, Front Axle Lateral Displacement Relative to Rail vs. Time (40.9 mph)

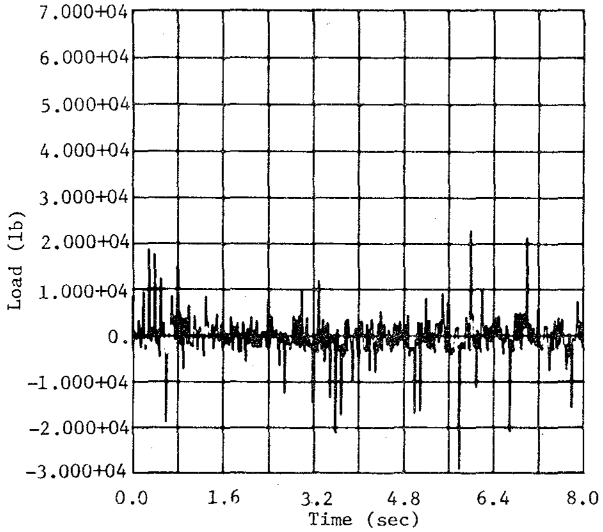

Figure 6-3 Front Truck, Front Axle/Wheel Lateral Force vs. Time (54.5 mph)

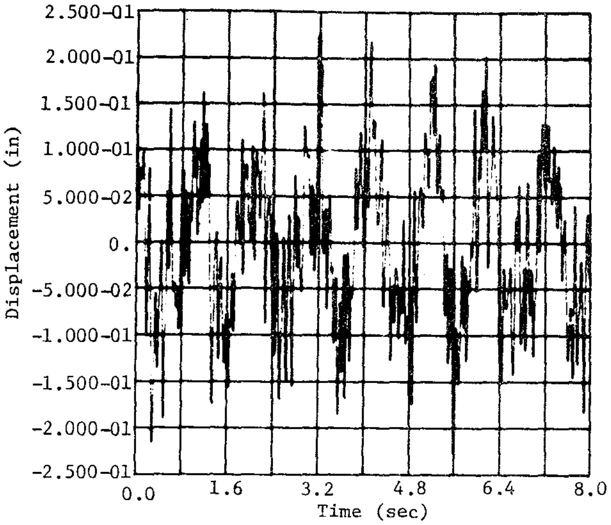

Figure 6-4 Truck, Front Axle Lateral Displacement Relative to Rail vs. Time (54.5 mph)

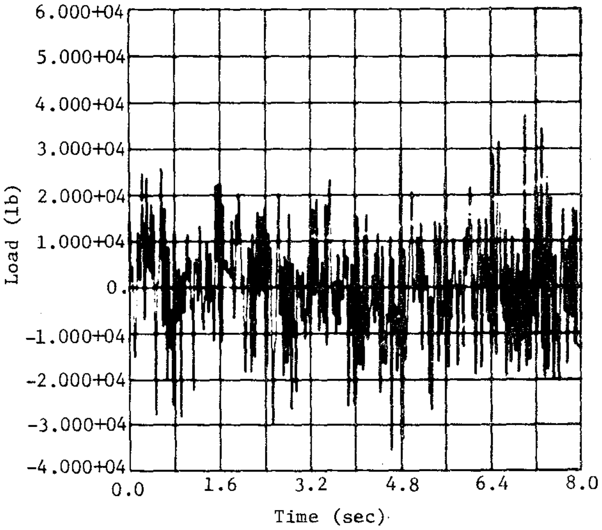

Figure 6-5 Front Truck, Front Wheel/Rail Lateral Force vs. Time (68 mph)

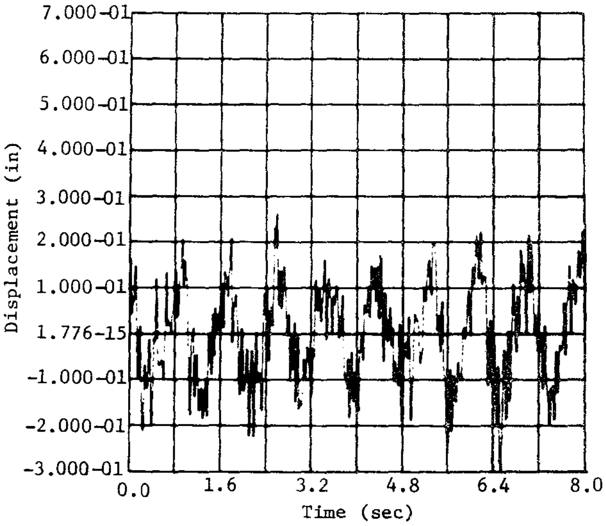

Figure 6-6 Front Truck Front Axle Lateral Displacement Relative to Rail vs. Time (68 mph)

1. Obtain RMS of test response data for comparison of analytical RMS.

2. Obtain PSD of test response data and calculate PSD of analytical responses for comparison of frequency content.

We are requesting test data in the required RMS and PSD form to make these comparisons.

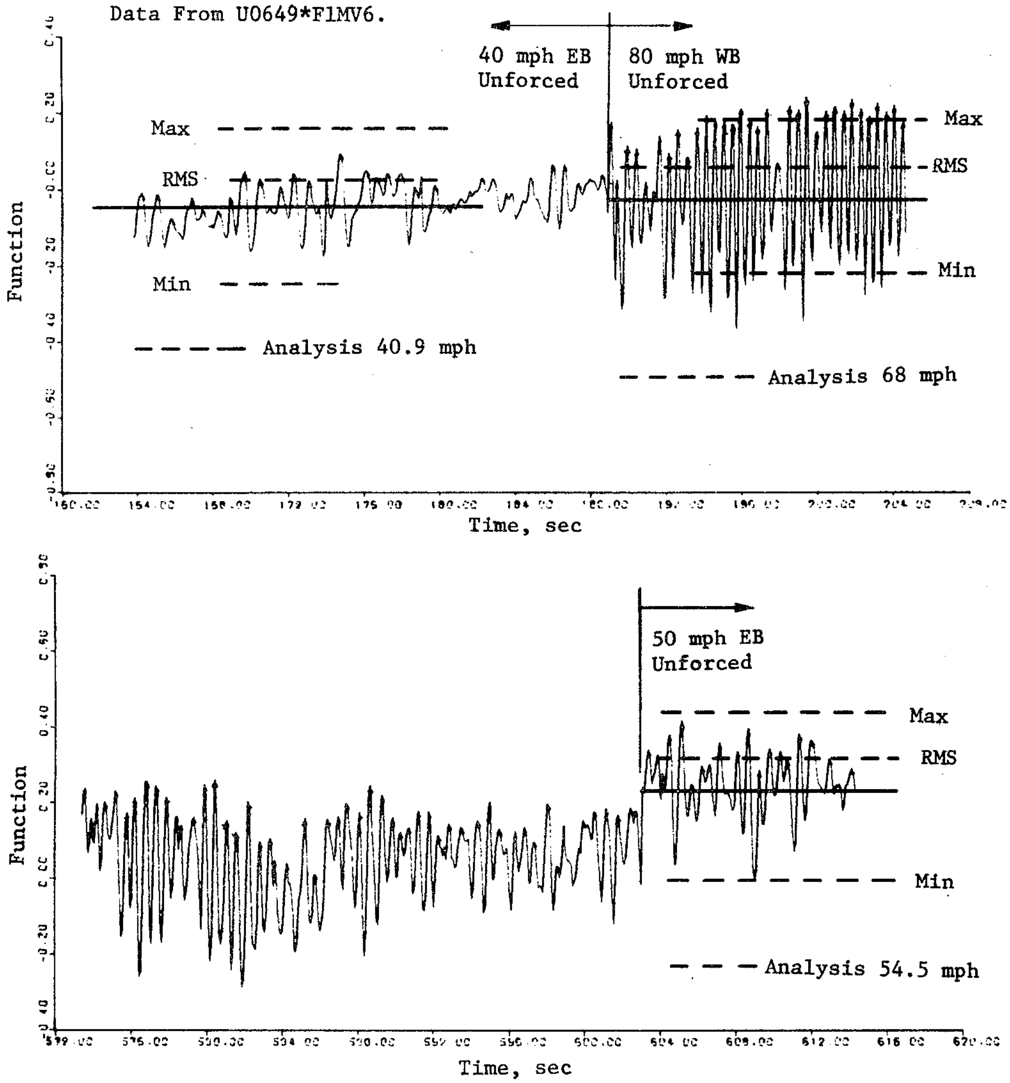

Figure 6-7 Measured Front Truck, Front Axle Displacement Relative to Rail

7.0 HUNTING STABILITY ANALYSES

It was stated earlier (Section 5) that wheel rail creep forces determine the model's hunting stability. These creep force terms were developed as Equation 5-16. It is intuitively clear that, if hunting can occur on perfectly regular track, the term $[KTC]\left\{h_t\right\}$ in Equation 5-16, cannot influence stability. That is, $\left\{h_t\right\} \equiv \left\{0\right\}$ for perfectly regular track. Consequently, this term may be deleted from Equation 6-1d when predicting hunting stability. It is known that hunting occurs only at specific speeds. Therefore, the forward velocity, V, which controls the coefficients [DC] in Equations 5-16 and 6-1c, is the parameter that must be varied in the analysis of hunting stability

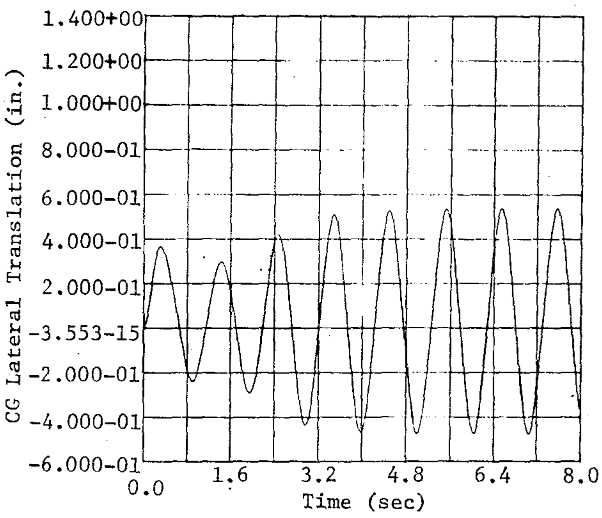

Figure 7-1 Car CG Lateral Translation, 60 fps

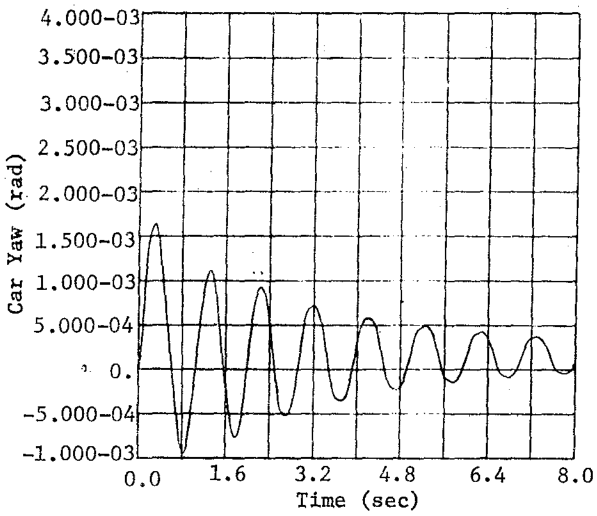

Figure 7-2 Car Yaw, 60 fps

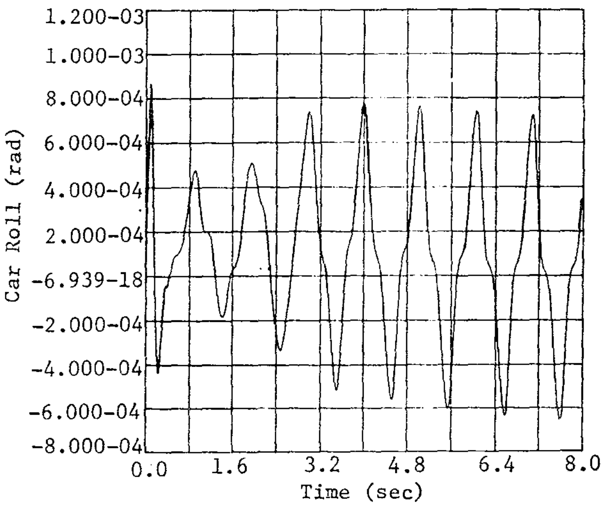

Figure 7-3 Car Roll, 60 fps

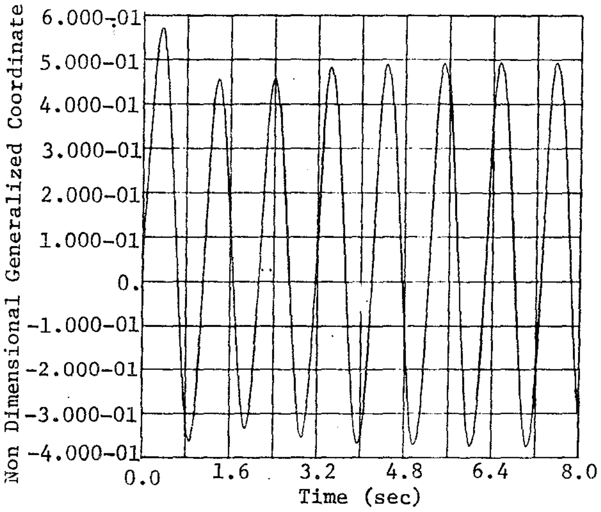

Figure 7-4 Front Truck Lateral Translation, 60 fps

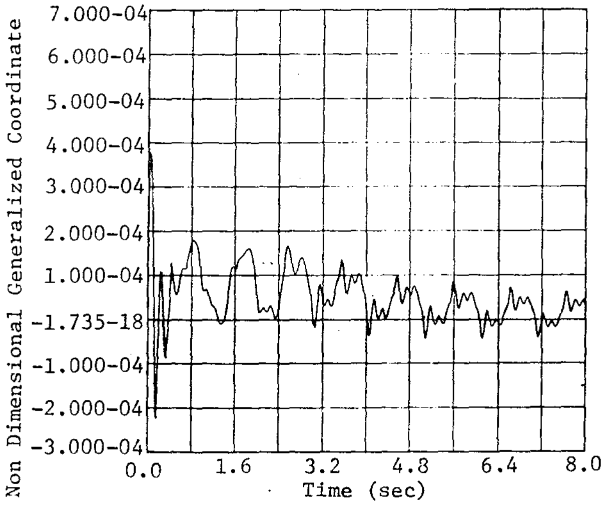

Figure 7-5 Car Torsion Mode (4.89 Hz), 60 fps

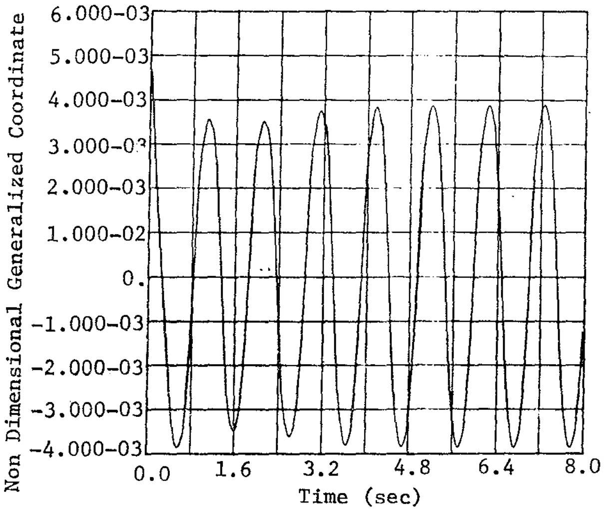

Figure 7-6 Front Truck Yaw, 60 fps

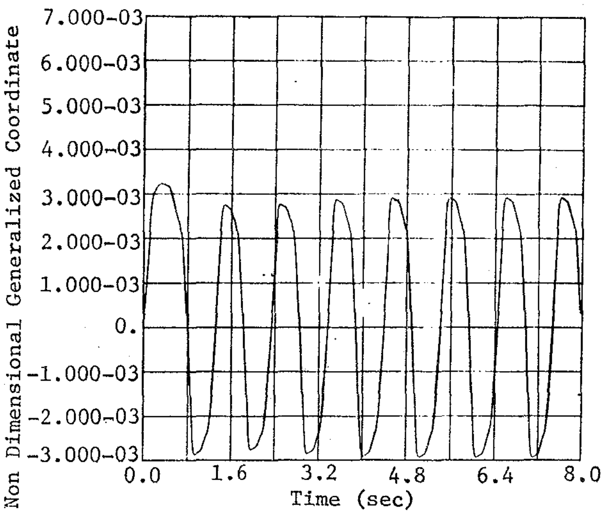

Figure 7-7 Front Truck Warping, 60 fps

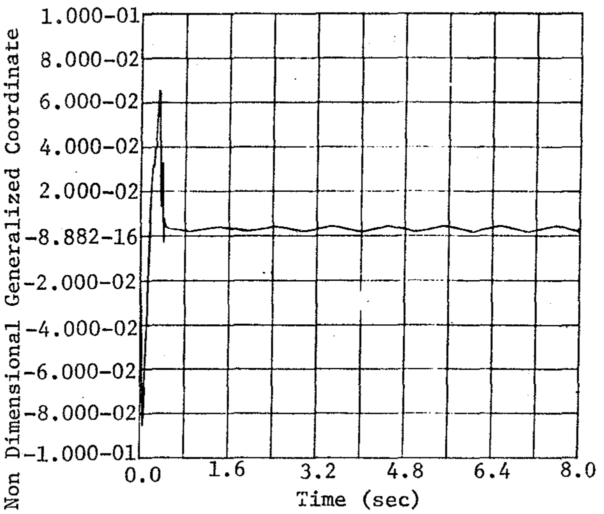

Figure 7-8 Front Truck Relative Lateral, 60 fps

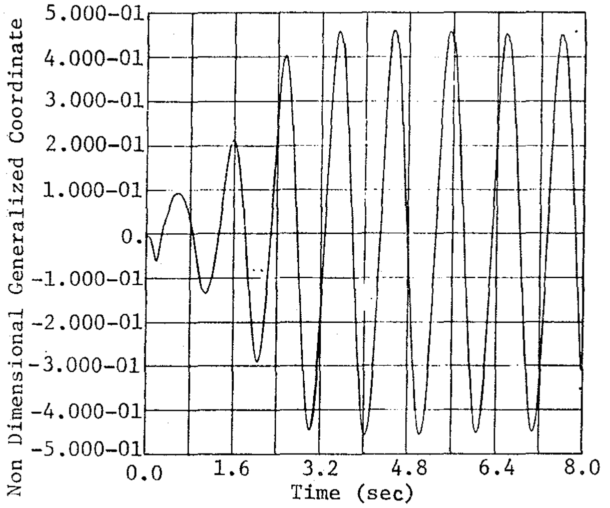

Figure 7-9 Rear Truck Lateral Translation, 60 fps

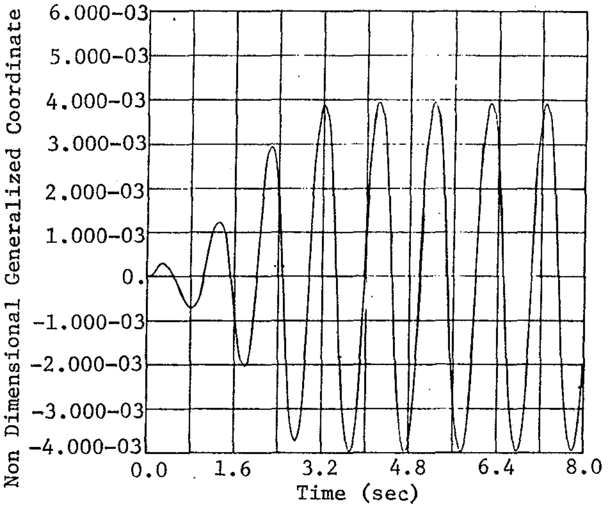

Figure 7-10 Rear Truck Yaw, 60 fps

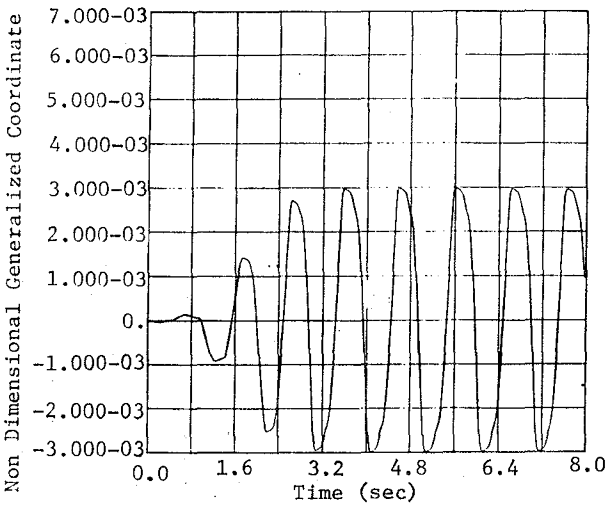

Figure 7-11 Rear Truck Warping, 60 fps

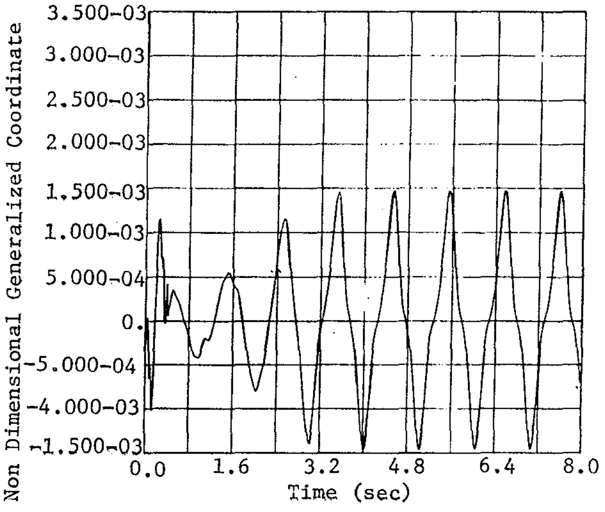

Figure 7-12 Rear Truck Relative Lateral, 60 fps

of a given vehicle configuration. The other obvious parameter is wheel conicity, α. However, our idealization of the creep forces is restricted to conical wheels. The more subtle wheel shape changes that result from wear were not considered in this study. Therefore, the nominal wheel conicity, 1:20, was used in all stability analyses.

Two approaches to the analysis of hunting stability were taken. First, the nonlinear model (Equation 6-1 with $\{h_t\} = \{0\}$) was given a set of initial displacements which exercise model nonlinearities, at some forward velocity, and a numerical integration scheme was used to obtain a time history of the response. A decaying response indicates stability. This analysis was repeated at forward velocities of 60fps (40.9mph), 80fps (54.4mph), and 100fps (68mph). Figures 7-1 through 7-12 present predicted responses of all carbody and ASF truck modes (front and rear) due to a 0.005 degree initial displacement of the front truck yaw mode while moving forward at 60fps (40.9mph). It can be seen that several modes build in amplitude from zero to some constant value. Similar results are obtained at the higher velocities, amplitude buildup increases somewhat with velocity.

This phenomenon is sometimes called limit cycling. This incipient instability at low amplitude, i.e., amplitude at which the model parameters are linear, indicates the existance of negative system damping at that frequency. That is, at small amplitudes in the linear range, the determinant of the system equations contains complex roots, λ, at least one of which has a positive real part. Mathematically, for the root

$$\lambda = n \pm i\omega \tag{7-1}$$

the response, R, has the form

$$R\ (t,\ \omega) = A\ (i\omega)\ e^{nt} \tag{7-2}$$

where

ω = system natural frequency in radians/s,

i = $\sqrt{-1}$,

$A(iw)$ = the complex amplitude of response.

If n is positive

$$\lim_{t \to \infty} R(t,\ \omega) \to \infty\ . \tag{7-3}$$

For a linear system, a standard complex eigensolution will yield all the system roots, thereby allowing assessment of stability. Therefore, our second approach was to linearize the car/truck model to allow the eigensolution. By restricting all motions to be less than Δ (see Figures 4-14 and -16), all spring rates, $k(q)$, in Equation 6-1b become linear. By replacing all coulomb dampers with equivalent viscous dampers, all damping terms, $f\left(\dot{q}_T\right)$, in Equation 6-1c become linear.

The equivalent viscous damper is obtained by equating the energy dissipated per cycle by coulomb friction to the energy dissipated per cycle by a viscous damper.

The dissipated energy (D.E.) is given by,

$$D.E. = -\int \text{Power}\ dt = -\int (\text{force x velocity})\ dt \tag{7-4}$$

For coulomb damping the force, f, is a constant so,

$$D.E._{\text{coulomb}} = -f\int \dot{q}dt \tag{7-5}$$

For viscous damping the force is the product of the damping coefficient, C, times velocity, so,

$$D.E._{\text{viscous}} = -C\int \dot{q}^2 dt \tag{7-6}$$

Figure 7-13 depicts a sinusoidal response as would be the case in the linear range, (i.e., $-\Delta \leq q \leq \Delta$) and defines the required integration for one-half cycle. Since the energy dissipated in one-half cycle is half the energy, we may equate Equations 7-5 and 7-6, substitute the values of the integrals from Figure 7-13, and solve for the equivalent damping coefficient, c, as,

$$C = \frac{4f}{\Delta\pi\omega} \tag{7-7}$$

Equation 7-7 implies that as $\Delta \to 0$, $c \to \infty$. However, we have seen from response of the nonlinear system that limit cycling occurs at amplitudes greater than the clearance, Δ. We conclude, then, that the lowest values of c, consistent with measure values of Δ are reasonable values for the linear model. The radial frequency, ω, is determined from the eigensolution of a model with zero structural damping, i.e., with all c = ω.

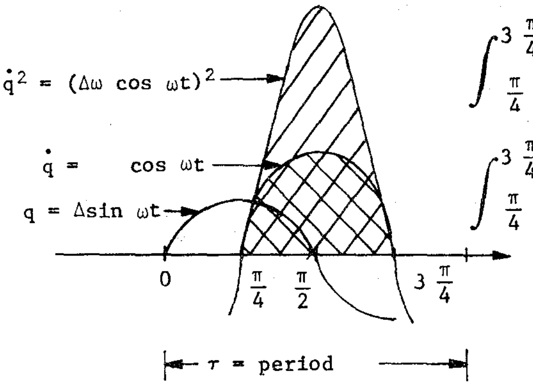

$$\int_{\frac{\pi}{4}}^{3\frac{\pi}{4}} \ddot q\, dt = \Delta^2\omega \qquad \int_{\frac{\pi}{4}}^{3\frac{\pi}{4}} \omega dt = -\frac{\Delta\omega^2\pi}{2}$$

$$\int_{\frac{\pi}{4}}^{3\frac{\pi}{4}} \dot q\, dt = \Delta \qquad \int_{\frac{\pi}{4}}^{3\frac{\pi}{4}} \cos \omega t = -2\Delta$$

Figure 7-13 Equivalent Damping Integrals

Figure 7-14 presents the full car/ASF truck/rail system closed loop damping ratios obtained for the linearized model from complex eigensolutions calculated at several forward velocities. System frequencies vs. forward velocity also are shown. Each frequency is associated with a system natural mode. Figures 7-15 and 7-16 present examples of these modes. Note that negative damping, and therefore hunting, is predicted over a broad range of speed, becoming progressively worse at higher speeds. However, these results cannot be interpreted as predicting complete instability since the missing nonlinear affects could result in a limit cycle at any speed, as was observed at 41 mph in the nonlinear analysis results.

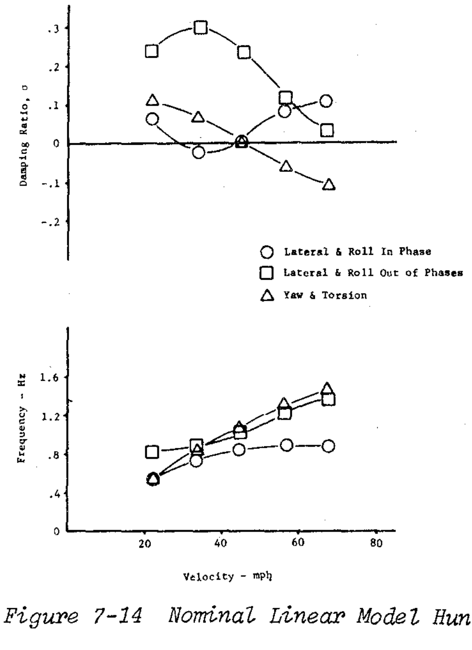

Figure 7-14 Nominal Linear Model Hunting

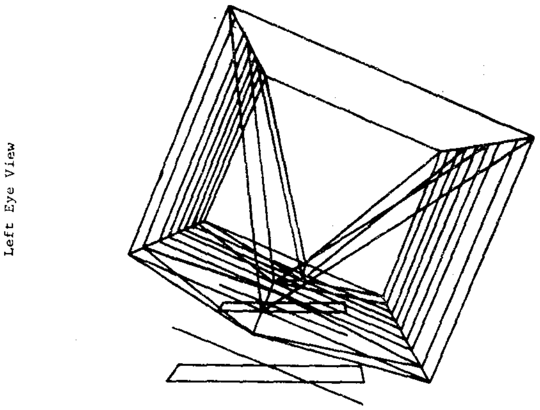

Full Car/Linear Trucks Hunting Model MF = 424.4 Model (6) = 1.25 Hz

Center of Eyes Location View Point Location Roll Angle = 180.0 Deg
X = 1.20000000E+03 X = 2.03000000E+02 Cone Angle = 2.0 Deg
Y = 0. Y = -0. Eye to Eye = 3.0 In.
Z = 7.00000000E+01 Z = -0.
Run No. = PLOTHM Date = 080C75

Figure 7-15 Roll Mode

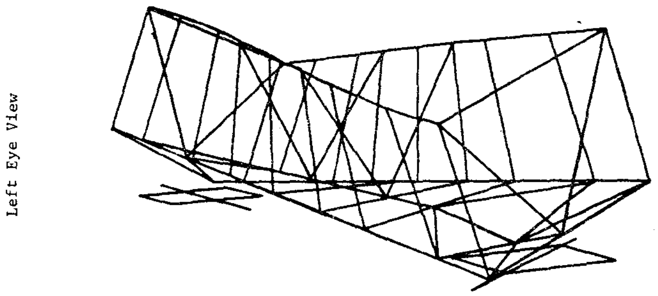

Full Car/Linear Trucks Hunting Model MF = 287.0 Model (9) = 3.76 Hz

Center of Eyes Location View Point Location Roll Angle = 180.0 Deg
X = 1.50000000E+03 X = 2.03000000E+02 Cone Angle = 20.0 Deg
Y = 7.00000000E+02 Y = -0. Eye to Eye = 3.0 In.
Z = 2.00000000E+02 Z = -0.
Run No. = PLOTHM Date = 080C75

Figure 7-16 Torsion Mode

8.0 CONCLUSIONS AND RECOMMENDATIONS

The objective of this study was to develop and verify a methodology for describing a mathematical model of an 80-ton open-hopper railcar system.

The objective was pursued as three subobjectives:

1) Modeling and verification of the car body.
2) Modeling and verification of the truck.
3) Verification of the car body/truck system.

It was concluded that state-of-the-art finite element modeling is a satisfactory methodology for characterizing unloaded railcar mode shapes, provided that careful attention is given to such details as weld continuity and eccentric sidewall loading. Also, a least squares distribution of lading mass allows calculation of good mode shapes for the loaded car. However, frequency description will generally require some minimal vibration test because of lading effects and/or wear on stiffness properties.

Truck modeling efforts led to the conclusion that modeling of individual truck joints is not practical. Rather, the mathematical analog of the principal deflection shapes of the truck, which has been described, provides a satisfactory methodology for truck modeling. Also, it was concluded that test conduct and instrumentation, and the analytical model definition is greatly simplified by the measurement of truck "mode" data. However, due to their highly nonlinear nature, the parameters of the analog can be determined only by test.

The last objective (verification of the carbody/truck system model) was pursued by comparing analytical time-domain response of the model to rail irregularities with operational responses, and by comparing hunting speeds predicted by the model with operational hunting speeds. It was concluded that time domain analyses using a linearized version of the car body/truck model could not be used to predict response to rail irregularities because the effects of the linearizing restraints on response cannot be estimated. Although further comparison with other statistical forms of operational test data are continuing, results to date lead us to conclude that the nonlinear model provides a satisfactory methodology for predicting order-of-magnitude values of responses to rail irregularities. However, theoretical/experimental correlation is not complete at this time. Thus, conclusions regarding the suitability of the model for use in hunting studies will be withheld until completion of the theoretical/experimental correlation studies.

In any event, only the nonlinear model is adequate for predicting order-of-magnitude limit cycle amplitudes occurring during hunting.

It is recommended that power spectral and statistical forms of measured data be obtained for comparison to corresponding forms of the analytical data. It is also recommended that a followup study of the carbody/truck model developed here be initiated with the objective of identifying the parameter interaction that causes the hunting so that this phenomenon can be minimized.

REFERENCES

1) R. L. Bispinghoff, H. Ashley, and R. L. Halfman; *Aeroelasticity*, Addison-Wesley Publishing Company, Inc., November 1957, pp. 114-124.
2) W. T. Thomson; *Vibration Theory and Application*, Prentice-Hall, Inc., 1966.
3) M. F. Rubinstein; *Matrix Computer Analysis of Structures*, Prentice-Hall, Inc., 1966.
4) R. Wohlen, W. Benfield, R. Philippus; *Evaluation of Modal Analysis Techniques*, Contract NAS8-26750, MCR-73-310, Martin Marietta Corporation, Denver, Colorado, December 1973.
5) American Steel Foundries Participation in AAR/RPI/FRA Track Train Dynamics Program - Parts 1-7.
6) Test Report Track-Train Dynamic Analysis and Test Program - Truck Static Test, November 1974 TR1315-74 Martin Marietta Corporation.
7) *Freight Car Dynamic Testing and Evaluation Report*. (To be published by E. Harry Law in March 1980). Contract DOT-OS-40018.